RSC Advances

PAPER

View Article Online
View Journal | View Issue

Cite this: *RSC Adv.*, 2025, **15**, 50633

Quinoline and coumarin isoxazole derivatives: synthesis, antitumor evaluation and molecular docking studies with Bcl-2

Martina Piškor, [a] Marina Ter,[a] Leentje Persoons, [b] Dirk Daelemans,[b] Ahmed Adel,[c] Mutasem O. Taha, [d] Astrid Milić,[e] Mirela Sedić[f] and Silvana Raić-Malić [a]*

Resistance to conventional therapies in pancreatic and hematologic malignancies highlights the need for novel agents that selectively induce tumor cell death. This study presents the design, synthesis, and evaluation of new quinoline- and coumarin-derived isoxazole analogs (**7a–e**, **8a–f**, **9a–e**) and their Re(I) and Ru(II) complexes (**7b$_{Re}$**, **9b$_{Re}$**, **7b$_{Ru}$**, **9b$_{Ru}$**). Antiproliferative assays against eight human cancer cell lines and noncancerous PBMCs identified quinoline amidoxime **8f** as particularly potent, with IC_{50} values of 2.1–4.7 μM against hematologic cancers (DND-41, HL-60, Z-138) and pancreatic adenocarcinoma (Capan-1), with selectivity indices of up to 48. Permeability and metabolic stability studies showed high membrane permeability and moderate clearance for **8f**. Molecular docking, validated by redocking of **J1Q** (PDB ID: 6QGK), confirmed that **8f** forms stable, energetically favorable complexes with Bcl-2 ($\Delta G\_bind = -84.98$ kcal mol^{-1}). These results support **8f** as a promising lead compound for further development as a selective Bcl-2-targeted anticancer agent.

Received 29th July 2025
Accepted 9th December 2025

DOI: 10.1039/d5ra05483d

rsc.li/rsc-advances

1. Introduction

Heterocycle quinolines[1–9] and coumarins[10–14] exhibit a broad spectrum of pharmacological activities, including anticancer activity. Mono- and bis-quinoline-based thiocarbohydrazones have shown efficacy against acute monocytic leukemia (THP-1) cells and pancreatic adenocarcinoma cancer stem cells, suggesting their capability to target multiple cellular mechanisms.[7] Similarly, 4-aminoquinolines have demonstrated notable anticancer activity against pancreatic carcinoma[6,8] with significant efficacy in xenograft models.6 Specifically, 4-aminoquinolines bearing a 6-methoxynaphthalene moiety have markedly increased pancreatic cancer cell cytotoxicity by suppressing the Akt/mTOR signaling pathway and inducing endoplasmic reticulum (ER) stress.[9] Quinoline-based compounds, particularly those functioning as protein kinase inhibitors, have been approved by the U.S. Food and Drug Administration (FDA) for clinical use (Fig. 1).[15–17] For example, bosutinib **I**, a dual inhibitor of Src and Abl kinases, is used for the treatment of Philadelphia chromosome-positive chronic myeloid leukemia (CML).[18–20]

Cabozantinib **II**, a multi-target receptor kinase inhibitor, has been approved for the treatment of thyroid and kidney cancers.[21] Its antiangiogenic properties are mediated through the inhibition of VEGFR and MET, which are critical for tumor vascularization.[22,23] Lenvatinib **III**, another multi-target kinase inhibitor, exhibits strong efficacy against growth factor receptors such as VEGFR, FGFR, and platelet-derived growth factor receptors. It is approved for the treatment of differentiated thyroid cancer.[2] Neratinib **IV**, approved for breast cancer treatment, irreversibly binds to the epidermal growth factor receptor (EGFR) and the human epidermal growth factor receptors HER2 and HER4.[24] In addition, the quinoline-based pelitinib (EKB-569) **V** is currently in phase II clinical trials as an irreversible EGFR inhibitor for colorectal and lung cancers.[25] Preclinical data show that dovitinib **VI** inhibits multiple kinases associated with various cancers, including acute myeloid leukemia (AML) and multiple myeloma,[26] while OSI-930 **VII** is designed to target both cancer cell proliferation and angiogenesis in selected tumors.[27]

Hybridization of bioactive organic components with metals has garnered significant interest in cancer research.[28,29] Transition metal complexes enhance conventional organic treatments through their structural flexibility, which allows them to adopt various chemical configurations and form effective

[a]*Department of Organic Chemistry, Faculty of Chemical Engineering and Technology, University of Zagreb, Marulićev trg 19, 10000 Zagreb, Croatia. E-mail: sraic@fkit.unizg.hr*

[b]*KU Leuven, Department of Microbiology, Immunology and Transplantation, Molecular Genetics and Therapeutics in Virology and Oncology Research Group, Rega Institute, 3000 Leuven, Belgium*

[c]*Faculty of Pharmacy and Medical Sciences, University of Petra, Amman 11196, Jordan*

[d]*Department of Pharmaceutical Sciences, Faculty of Pharmacy, University of Jordan, Amman 11942, Jordan*

[e]*Selvita d.o.o., Zagreb 10000, Croatia*

[f]*Centre for Applied Bioanthropology, Institute for Anthropological Research, Zagreb, Croatia*

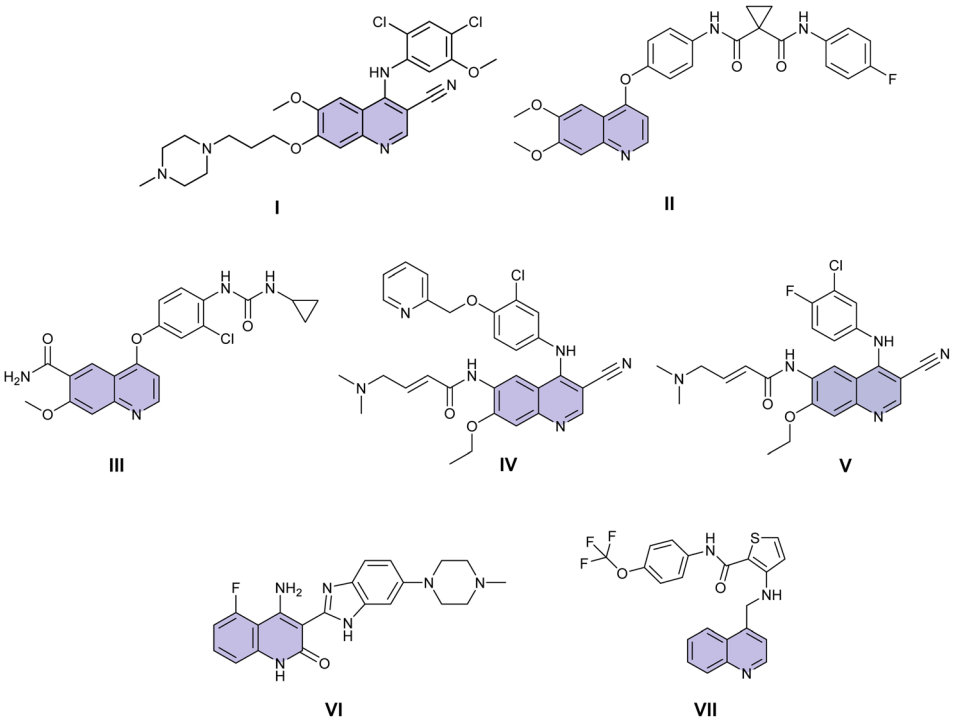

Fig. 1 Representative quinoline-based kinase inhibitors approved for cancer therapy (I–IV) or under clinical investigation (V–VII).

binding interactions with target biomolecules, significantly increasing their therapeutic efficacy.[28,30,31]

Research has particularly focused on ruthenium, titanium, and gold based anticancer agents, some of which have shown promising results in phase I and II clinical trials.[32,33] In addition, rhenium-based complexes, particularly those featuring stable rhenium(I) tricarbonyl motifs, are emerging as promising theranostics due to their kinetic stability and versatile

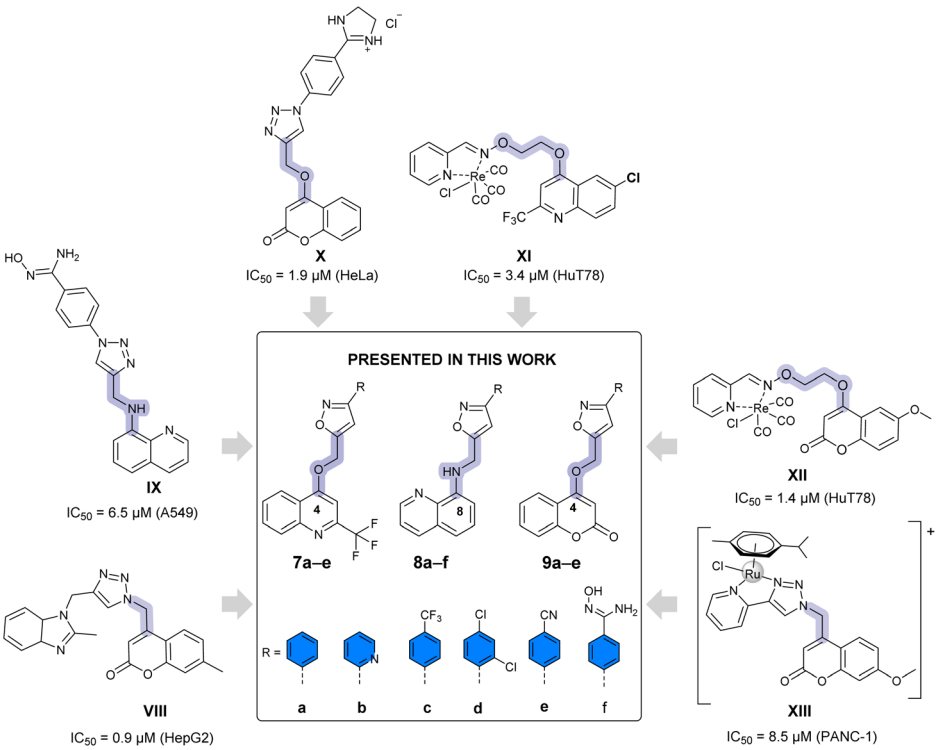

Fig. 2 Designed quinoline (7a–e, 8a–f) and coumarin (9a–e) derivatives of 3-aryl-substituted isoxazoles with oxymethylene and aminomethylene linker.

spectroscopic properties.[34,35] Metal complexes containing quinoline and coumarin moieties have shown significant cytotoxic activity against various cancer cell lines.[36–41]

In our previous studies, the 4-substituted 1,2,3-triazole-coumarin hybrid **VIII** exhibited strong and selective antiproliferative effects on hepatocellular carcinoma cells (HepG2), associated with inhibition of 5-lipoxygenase (5-LO) activity and disruption of sphingolipid signaling through interference with intracellular acid ceramidase (ASAH) activity.[42] The amidoxime-substituted quinoline 1,2,3-triazole **IX** linked *via* an aminomethylene linker demonstrated notable activity against lung adenocarcinoma cells (A549), whereas the amidino-substituted coumarin 1,2,3-triazole **X** containing an oxymethylene linker exhibited activity against cervical cancer cells (HeLa) and selective nucleic acid binding through intercalative and minor-groove interactions.[43] The tricarbonyl Re(I) complexes of quinoline **XI** (IC_{50} = 3.4 μM) and coumarin **XII** (IC_{50} = 1.4 μM) aldoxime ether ligands promoted ROS generation, mitochondrial membrane depolarization, and G0/G1 cell-cycle arrest in T-cell lymphoma cells (HuT78), while the Ru(II) half-sandwich complex containing a coumarin-1,2,3-triazole ligand **XIII** induced downregulation of AKT and ERK signaling pathway in pancreatic cancer cells (PANC-1) and reduced intracellular levels of reactive oxygen species.[41,44]

Building on the aforementioned findings and our previous work on the development of quinoline[43–46] and coumarin[41,42,44,47] derivatives, we designed a new series of quinoline and coumarin derivatives bearing 3-aryl-substituted isoxazole core connected through oxymethylene and aminomethylene linkers (Fig. 2) to evaluate their anticancer activity in eight malignant cancer cell lines and assess their cytotoxicity in normal cells using peripheral blood mononuclear cells (PBMCs) from two healthy donors. The metabolic stability and permeability of selected compounds exhibiting potent antiproliferative activity were further assessed. Additionally, molecular docking studies were conducted to explore the potential anticancer mechanisms of these selected compounds as novel Bcl-2 inhibitor.

2. Results and discussion

2.1. Synthesis and structural characterization

Following the synthetic strategy outlined in Scheme 1, a series of quinoline (**7a–e**, **8a–f**) and coumarin (**9a–e**) derivatives with oxymethylene- and aminomethylene-linked isoxazole were synthesized *via* a 1,3-dipolar cycloaddition reaction. This reaction involved the corresponding propargylated quinoline (**4**, **5**) or coumarin (**6**) derivatives and various nitrile oxides, as illustrated in Scheme 1. The main starting materials, 4-

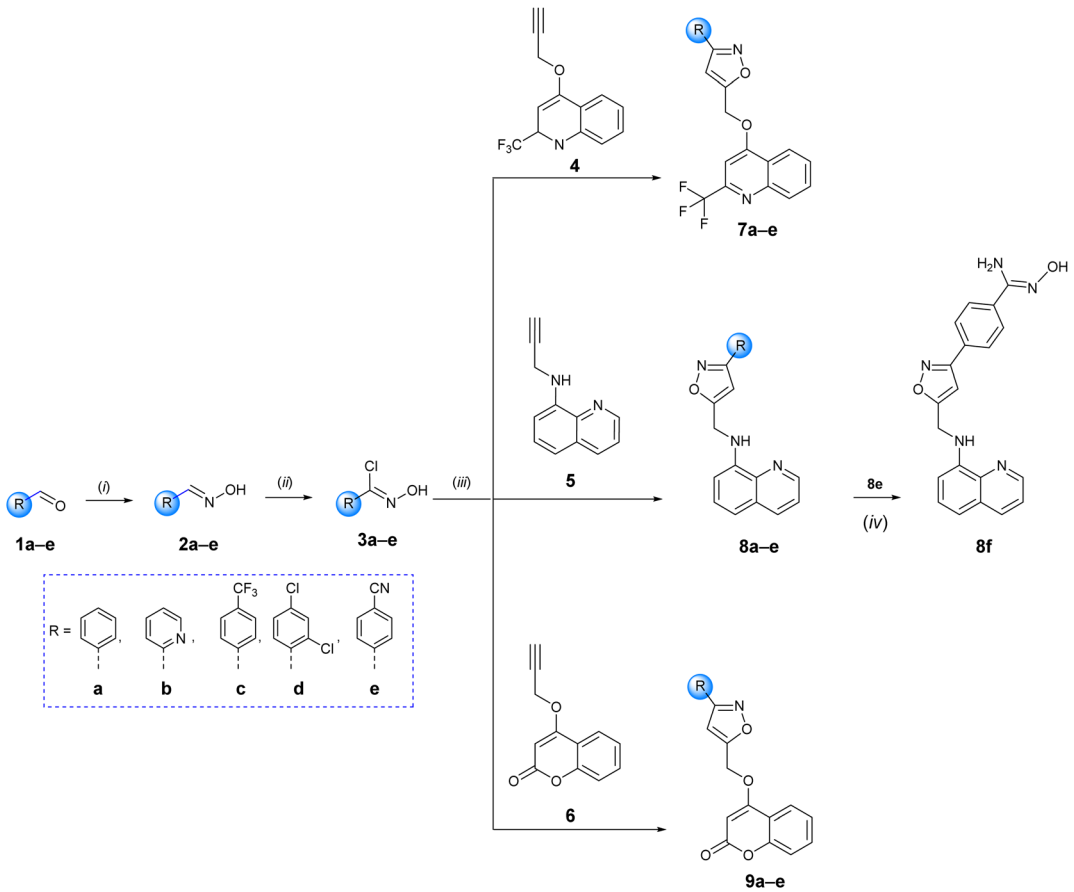

Scheme 1 Synthesis of quinoline (**7a–e**, **8a–f**) and coumarin (**9a–e**) isoxazole derivatives with oxymethylene and aminomethylene linkers. Reagents and conditions: (i) $NH_2OH \times HCl$, $CH_3OH : H_2O$ = 8 : 1, 5–30 min, r.t., under ultrasound irradiation; (ii) NCS, DMF, 4–12 h, 60 °C; (iii) Et_3N, CH_2Cl_2, 12 h, reflux; (iv) methanol : DMF = 2 : 1, $NH_2OH \times HCl$, Et_3N, 6 h, 100 °C.

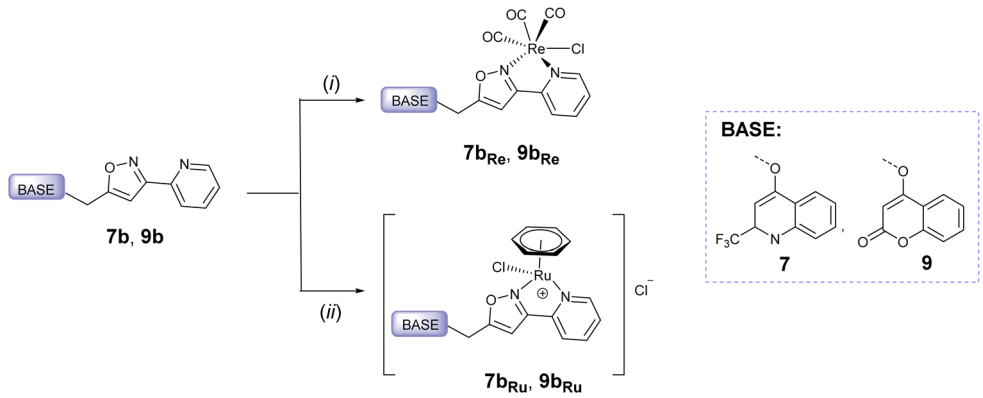

Scheme 2 Synthesis of Re(I) (**7b$_{Re}$**, **9b$_{Re}$**) and Ru(II) (**7b$_{Ru}$**, **9b$_{Ru}$**) complexes with pyridine–isoxazole ligands **7b** and **9b**. Reagents and conditions: (i) $Re(CO)_5Cl$, $CHCl_3$, reflux, 12 h; (ii) $[Ru(benzene)Cl_2]_2$, EtOH, 24 h, r.t.

hydroxycoumarin and 8-aminoquinoline, were commercially available, while 4-(trifluoromethyl)quinolin-4-ol was synthesized *via* the Conrad–Limpach cyclocondenzation of aniline and ethyl 4,4,4-trifluoroacetoacetate in polyphosphoric acid.[45] The *O*-propargylation of 4-hydroxycoumarin and 2-(trifluoromethyl) quinolin-4-ol, as well as the *N*-propargylation of 8-aminoquinoline were carried out under similar conditions using K_2CO_3 as a base and an excess of propargyl bromide, as described in the literature.[43,45,46] The nitrile oxides, which served as dipoles in the cycloaddition, were generated *in situ* from *N*-hydroxybenzimidoyl chloride **3a–e** under basic conditions (Et_3N).

The synthesis of *N*-hydroxybenzimidoyl chlorides was achieved through a two-step protocol. First, aldehydes **1a–e** were used as precursors for the synthesis of aldoximes **2a–e**, which were subsequently converted to the corresponding *N*-hydroxybenzimidoyl chlorides **3a–e** using *N*-chlorosuccinimide (NCS) in *N*,*N*-dimethylformamide at elevated temperatures, as shown in Scheme 1.[48–52] In the final step, a regioselective 1,3-dipolar cycloaddition reaction was performed between *in situ* generated nitrile oxides and corresponding alkynes **4–6** in the presence of triethylamine in dichloromethane, yielding the targeted 3,5-disubstituted isoxazoles in moderate to high yields (42–95%). The nitrile derivative **8e** served as a precursor for the synthesis of amidoxime-substituted quinoline derivative **8f** as shown in Scheme 1. In addition, 2-(trifluoromethyl)quinoline (**7b**) and coumarin (**9b**) with 3-(pyridinyl)isoxazole were subsequently used as bidentate ligands for the preparation of rhenium(I) and ruthenium(II) complexes (Scheme 2). Rhenium(I) complexes were efficiently synthesized by complexation with pentacarbonylrhenium(I) chloride, yielding the tricarbonyl

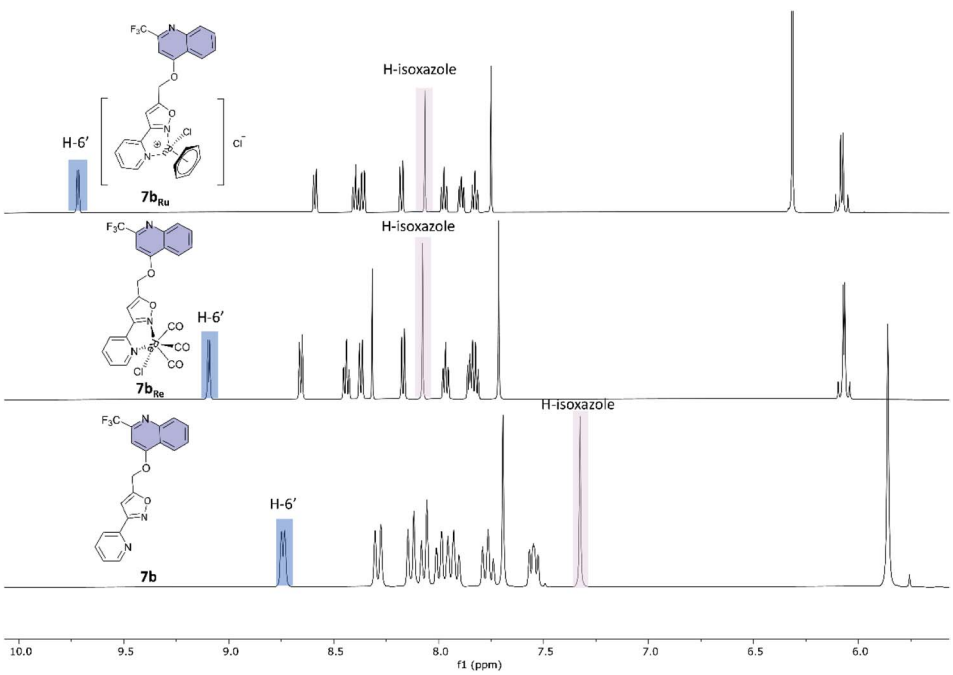

Fig. 3 Proton NMR spectra comparison of ligand **7b**, rhenium(I) tricarbonyl complex **7b$_{Re}$** and ruthenium-phenyl complex **7b$_{Ru}$** in DMSO-d_6, highlighting major proton signal shifts upon metal coordination.

Table 1 *In vitro* antiproliferative activity of quinoline (**7a–e**, **8a–f**) and coumarin derivatives (**9a–e**), along with their rhenium(I) (**7bRe**, **9bRe**) and ruthenium(II) complexes (**7bRu**, **9bRu**)

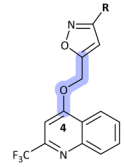

7a–e, 7b$_{Re}$, 7b$_{Ru}$

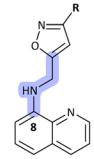

8a–f

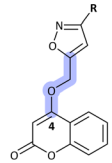

9a–e, 9b$_{Re}$, 9$_{Ru}$

		IC$_{50}$[a] (μM)													
														PBMC	
Cmpd	R	Capan-1	SI[b] (Capan-1)	HCT-116	LN229	NCI-H460	DND-41	SI[c] (DND-41)	HL-60	SI[d] (HL-60)	K562	Z-138	SI[e] (Z-138)	Donor 1	Donor 2
7a		7.4	>13.5	>100	32.1	>100	65.2	>1.5	>100	—	>100	68.2	>1.5	>100	>100
7b		>100	—	>100	>100	>100	>100	—	>100	—	>100	>100	—	>100	>100
7b$_{Re}$		8.3	>2.3	>100	32.1	33.0	8.2	>2.4	7.2	>2.7	9.6	5.0	>3.9	19.4	29.8
7b$_{Ru}$		>100	—	>100	>100	>100	>100	—	>100	—	>100	>100	—	>100	>100
7c	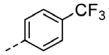	>100	—	>100	>100	>100	>100	—	>100	—	>100	>100	—	>100	>100
7d	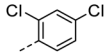	>100	—	>100	>100	>100	>100	—	>100	—	>100	>100	—	>100	>100
7e	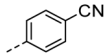	22.5	>4.1	>100	23.9	>100	43.7	>2.1	62.2	>1.5	83.2	36.7	>2.5	91.3	>100
8a		11.4	>8.8	>100	33.7	>100	>100	—	79.6	>1.3	>100	35.3	>2.8	>100	>100
8b		13.1	>7.6	>100	22.8	>100	44.3	>2.3	64.8	>1.5	79.7	28.2	>3.5	>100	>100
8c	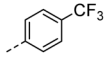	19.9	>5.0	>100	51.8	>100	82.3	>1.2	>100	—	>100	85.9	>1.2	>100	>100
8d	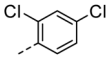	14.9	>6.7	>100	54.4	>100	53.9	>1.9	67.1	>1.5	33.0	27.9	>3.6	>100	>100
8e	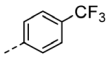	13.1	>7.6	>100	27.2	>100	15.3	>6.5	16.5	>6.1	11.1	10.8	>9.3	>100	>100
8f	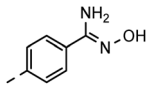	4.7	>21.3	>100	15.6	95.1	2.3	>43.5	2.8	>35.7	86.6	2.1	>47.6	>100	>100
9a		>100	—	>100	>100	>100	>100	—	>100	—	>100	>100	—	>100	>100
9b		>100	—	−>100	>100	>100	>100	—	>100	—	>100	>100	—	>100	>100
9b$_{Re}$		27.7	>0.4	55.2	62.4	>100	11.3	>0.9	31.2	>0.32	21.9	9.1	>1.1	11.4	10.1

Table 1 (*Contd.*)

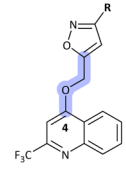

7a–e, 7b$_{Re}$, 7b$_{Ru}$

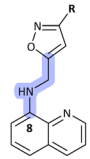

8a–f

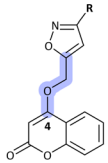

9a–e, 9b$_{Re}$, 9$_{Ru}$

		IC$_{50}$[a] (μM)													
														PBMC	
Cmpd	R	Capan-1	SI[b] (Capan-1)	HCT-116	LN229	NCI-H460	DND-41	SI[c] (DND-41)	HL-60	SI[d] (HL-60)	K562	Z-138	SI[e] (Z-138)	Donor 1	Donor 2
9b$_{Ru}$		>100	—	>100	>100	>100	>100	—	>100	—	>100	>100	—	>100	>100
9c	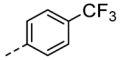	>100	—	>100	>100	>100	>100	—	>100	—	>100	>100	—	>100	>100
9d	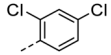	80.1	1.3	>100	>100	>100	>100	—	>100	—	>100	>100	—	>100	>100
9e	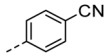	>100	—	>100	>100	>100	>100	—	>100	—	>100	>100	—	>100	>100
Etoposide		Etoposide	>10 000	0.59	0.02	0.69	0.05	>2000	0.03	>3333	0.03	0.03	>3333	>100	>100

[a] IC$_{50}$ – compound concentration that inhibited cell growth by 50%. [b] Selectivity index towards pancreatic adenocarcinoma cells (Capan-1), SI = [IC$_{50}$ PBMC]/[IC$_{50}$ Capan-1]. [c] Selectivity index towards T-cell leukemia cells (DND-41), SI = [IC$_{50}$ PBMC]/[IC$_{50}$ DND-41]. [d] Selectivity index towards acute myeloid leukemia cells (HL-60), SI = [IC$_{50}$ PBMC]/[IC$_{50}$ HL-60]. [e] Selectivity index towards non-Hodgkin's lymphoma (Z-138), SI = [IC$_{50}$ PBMC]/[IC$_{50}$ Z-138].

complexes $7b_{Re}$ and $9b_{Re}$ with high yields (>80%). In contrast, the formation of ruthenium(II) complexes $7b_{Ru}$ and $9b_{Ru}$ using $[Ru(benzene)Cl_2]_2$ as metal precursor resulted in comparatively lower yields (<30%).

All complexes were characterized by NMR (Fig. S1–S20), IR (Fig. S21–S26), and UV/Vis (Fig. S27–S32) spectroscopy. ^{1}H NMR and ^{13}C NMR spectroscopy confirmed the purity of the synthesized complexes and ligands. Signal assignments were based on chemical shifts, coupling constants and splitting patterns, which showed excellent agreement with the proposed molecular structures. Significant differences were observed between the NMR spectra of the uncoordinated ligands and their corresponding rhenium and ruthenium complexes, characterized by pronounced deshielding of certain proton signals (Fig. 3).

In the free ligand **7b**, the pyridyl H-6′ proton appeared as a downfield doublet at 8.74 ppm, while the isoxazole proton was observed at 7.69 ppm. Upon coordination with rhenium, the H-6′ signal shifted further downfield to 9.09 ppm, and the isoxazole proton shifted to 8.07 ppm, indicating metal–N bond formation.[44,53] Coordination with ruthenium resulted in an even stronger downfield shift of the H-6′ signal to 9.71 ppm, reflecting greater deshielding due to the interaction with the ruthenium ion.[41] Interestingly, the isoxazole proton in the ruthenium complex exhibited a similar shift to that in the rhenium complexes, appearing at 8.06 ppm (Fig. 3). The ^{13}C NMR spectra of the rhenium(I) and ruthenium(II) complexes also showed downfield shifts, which can be attributed to changes in the carbon environment during coordination. In addition, the spectra of the rhenium complexes $7b_{Re}$ and $9b_{Re}$ showed three characteristic signals corresponding to carbonyl groups, appearing in the range of 187–198 ppm, indicating the presence of $[Re(CO)_3Cl]$ in the structures. The IR spectra of the ligands showed complex patterns due to overlapping stretching bands of the chemical bonds in the pyridine, isoxazole, coumarin or quinoline rings. Coordination with rhenium resulted in pronounced, strong ν(CO) stretching bands, both symmetric and asymmetric, characteristic of *fac*-$[Re(CO)_3Cl]$ groups observed in the range of 2031–1889 cm^{-1}.[54]

2.2.1. Antiproliferative activity. The antiproliferative potential of novel quinoline- (**7a–e**, **8a–f**) and coumarin-based isoxazole derivatives (**9a–e**) was investigated across a series of human tumor cell lines (Table 1). These included pancreatic adenocarcinoma (Capan-1), colorectal carcinoma (HCT-116), glioblastoma (LN-229), small cell lung cancer (NCI-H460), T-cell leukemia (DND-41), acute myeloid leukemia (HL-60), chronic myeloid leukemia (K562) and non-Hodgkin's lymphoma (Z-138). Non-cancerous peripheral blood mononuclear cells (PBMCs) from two healthy donors were included as non-cancerous cells to assess selectivity. Etoposide was used as the reference drug. Comparative analysis of the antitumor activities of 2-(trifluoromethyl)quinolines **7a–e**, quinoline **8a–f** and, coumarin derivatives **9a–e** revealed significant differences in their antiproliferative effects. Generally, quinoline-based compounds demonstrated more pronounced antitumor activity compared to coumarin analogs. Among 2-(trifluoromethyl)quinolines with an oxymethylene linker between quinoline and aryl-substituted isoxazole, quinoline **7a** with phenyl-substituted isoxazole showed strong growth-inhibition (IC_{50} = 7.4 μM) against pancreatic adenocarcinoma cells (Capan-1) and moderate inhibition of glioblastoma (LN229), T-cell leukemia (DND-41) and non-Hodgkin's lymphoma (Z-138). In contrast, its quinoline congener **7b** with pyridinyl-substituted isoxazole did not exhibit any antiproliferative effects. Quinoline **7e** with *p*-cyanophenyl showed moderate growth inhibition across all human tumor cell lines, except for HT-116 and NCI-H460 cell lines. Quinoline derivatives **8a–f** with an aminomethylene linker showed significant antiproliferative potential and selective activity, particularly against Capan-1, LN-299, DND-41, HL-60 and Z-138 cell lines. These compounds were non-cytotoxic to non-cancerous PBMC cells. Notably, (4-amidoxime)phenyl-substituted **8f** showed the most significant activity, with IC_{50} values of 4.7 μM, 2.3 μM, 2.8 μM and 2.1 μM against Capan-1, DND-41, HL-60 and Z-138 cell lines, respectively, and selectivity indices (SI) ranging from 21 to 48. Coordination with rhenium(I) significantly enhanced the antiproliferative activity of both $7b_{Re}$ and $9b_{Re}$, while ruthenium(II) complexes $7b_{Ru}$ and $9b_{Ru}$ exhibited no such activity. Among the rhenium(I) tricarbonyl complexes, coumarin Re(I) complex $9b_{Re}$ showed the most potent antiproliferative effects against hematologic malignancies, such as DND-41, HL-60, K562 and Z-138 cell lines, with IC_{50} values of 11.3 μM, 31.2 μM, 21.9 μM and 9.1 μM, respectively. Its quinoline analog $7b_{Re}$ exhibited even stronger antitumor activity against DND-41, HL-60, K562 and Z-138 cell lines with IC_{50} values of 8.2 μM, 7.2 μM, 9.6 μM and 5.0 μM, respectively. In addition, $7b_{Re}$ displayed significant growth inhibition (IC_{50} = 8.3 μM) in pancreatic cancer cells (Capan-1). However, both rhenium organometallic complexes $7b_{Re}$ and $9b_{Re}$ were also cytotoxic to non-cancerous PBMC cells. Conversely, quinoline (**7a–e**, **8a–f**) and coumarin isoxazole (**9a–e**) derivatives were non-cytotoxic to non-cancerous cells.

2.2.2. Metabolic stability and permeability. The metabolic stability in mouse liver microsomes and permeability on MDCKII-hMDR1 cell monolayers were experimentally investigated for selected derivatives **7a**, **7b**, $7b_{Re}$ and **8a–8f**, which exhibited the most potent antitumor activity (Table 2). These properties are key factors for oral bioavailability and are routinely assessed during early drug discovery to optimize pharmacokinetic profiles.[55] Metabolic studies showed that compounds **7a**, **7b**, **8a** and **8b** exhibited high clearance rates (>70% liver blood flow, LBF), indicating rapid metabolism and elimination. This highlights the influence of phenyl and pyridinyl substituents on the isoxazole moiety in modulating metabolic stability. In contrast, derivatives **8d**, **8e**, and **8f** with 2,4-dichlorophenyl, 4-cyanophenyl and (4-amidoxime)phenyl-substituted isoxazole exhibited moderate clearance rates (30–70% LBF), suggesting a balanced metabolic profile.

Quinolines **7a**, **7b**, $7b_{Re}$, **8a**, and **8c–e** showed low to moderate membrane permeability, which may limit their oral bioavailability. In contrast, quinolines **8b** and **8f** containing pyridine and (4-amidoxime)phenyl substituents exhibited high permeability, indicating strong potential for oral absorption and bioavailability. Efflux measurements revealed low efflux activity for most compounds, indicating limited interaction

Table 2 Permeability and metabolic stability of representative compounds **7a**, **7b**, **7bR$_e$**, and **8a–f**

Cmpd	% LBF predicted *in vivo* hepatic clearance	Clearance classification[a]	P_{app} (AB)[b] [$\times 10^{-6}$ cm s^{-1}]	P_{app} (BA)[c] [$\times 10^{-6}$ cm s^{-1}]	Efflux ratio	Permeability[d]/ efflux[e] classification
7a	74	High	<0.1	0.1	N/A	Low/—
7b	87	High	6.5	4.6	0.7	Moderate/low
7b$_{Re}$	55	Moderate	<0.1	1.4	>13.0	Low/high
8a	>97	High	1.7	N/A	N/A	Low/—
8b	96	High	17.2	27.8	1.6	High/low
8c	N/A	N/A	<0.1	<0.1	N/A	Low/—
8d	51	Moderate	<0.1	<0.1	N/A	Low/—
8e	55	Moderate	3.6	3.1	0.9	Moderate/low
8f	53	Moderate	15.0	13.7	0.9	High/low

[a] Clearance classification; CL <30% low, 30–70% moderate, and >70% high. [b] Apparent permeability coefficient in the apical-to-basolateral direction. [c] Apparent permeability coefficient in the basolateral-to-apical direction. [d] Permeability classification: <2 low, 2–10 moderate, >10 high. [e] Efflux classification: <2 no efflux, >2 active efflux.

with efflux transporters. This suggests that these compounds may have better intracellular retention, enhancing their therapeutic efficacy. Overall, these data suggest that quinolines **8b** and **8f** are promising candidates for further development due to their high permeability and moderate clearance rates, which are favorable for oral bioavailability and therapeutic effectiveness.

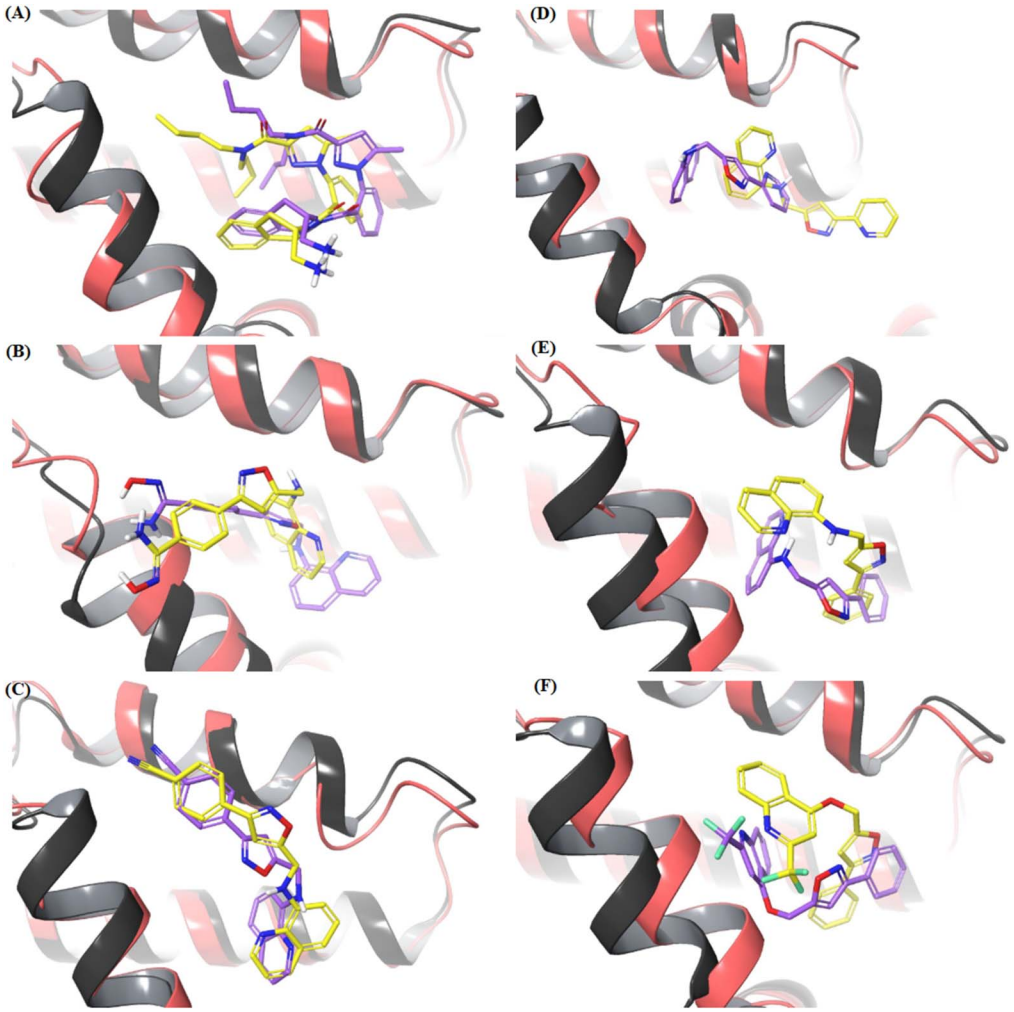

Fig. 4 Structure overlays comparing the first (grey) and last (red) frames from a 1000 ns MD simulation study of the following complexes: (A) co-crystallized complex of **J1Q** with Bcl-2 (PDB code: 6QGK), (B)–(F): the virtual complexes of **7a**, **8a**, **8b**, **8e** and **8f**, respectively (Purple ligands represent the first frame while yellow represents the last frames).

2.2.3. Molecular modeling studies on Bcl-2 interaction. The Bcl-2 protein, a prominent member of the Bcl-2 family, is a well-known antiapoptotic regulator that inhibits programmed cell death (apoptosis) by forming heterodimers with pro-apoptotic protein BAX. Bcl-2 promotes cell survival by regulating intracellular calcium (Ca^{2+}) concentrations and exerting antioxidant effects.[56] Given its critical role in apoptosis regulation, Bcl-2 is an attractive target for the development of novel anticancer drugs. Various quinoline-based compounds have been described as effective Bcl-2 inhibitors capable of inducing apoptosis in cancer cells. For instance, quinoline-based oxadiazole analogs have demonstrated sub-micromolar antiproliferative activity in Bcl-2-expressing cancer cell lines, attributed to their Bcl-2 inhibitory properties.[57] Another quinolone derivative, namely 6-methoxy-2-(3,4,5-trimethoxy-benzenesulfonyl)-quinolin-5-ylamine (B392) exerts anticancer effects in leukemic cell lines by inducing phosphorylation of Bcl-2, thereby modulating its antiapoptotic function.[58,59] Similarly, isoxazole-based compounds have shown anticancer efficacy through Bcl-2 inhibition. For example, the cytotoxic effect of isoxazole-curcumin in breast cancer cells was found to be associated with its ability to bind Bcl-2, as revealed by molecular docking studies.[60] These studies collectively suggest that quinoline and isoxazole-based derivatives hold promise as Bcl-2 targeted anticancer agents. Prompted by these studies, we investigated the potential interaction between the most potent compounds identified in this study and Bcl-2 through molecular docking and molecular dynamics (MD) simulations.[61] Based on the antiproliferative activity profile (Table 1) and selectivity patterns, particularly for compound **8f**, Bcl-2 was identified as a plausible target. Docking studies were conducted using Glide SP, validated by successfully re-docking the known inhibitor **J1Q** (PDB: 6QGK, $IC_{50} = 1.3$ μM, ChEMBL ID: CHEMBL4438456) with an RMSD of 0.45 Å (Fig. S33, SI). The Bcl-2 complexes of the most bioactive compounds **7a**, **8a**, **8b**, **8e** and **8f**, along with the crystallographic complex of the reference inhibitor **J1Q** (PDB code: 6QGK), were subjected to 1000 ns MD simulations using Desmond package within Schrödinger suite to assess binding affinities and dynamic stability.

Fig. 4 shows structure overlays comparing the first and last frames from a 1000 ns MD simulation study of the evaluated complexes. Several metrics were analyzed to assess the stability and binding affinities of the Bcl-2 complexes. These included the root-mean-square deviation (RMSD) of the protein backbone to evaluate complex stability, the root-mean-square fluctuation (RMSF) of residue side chains and ligand atoms to determine flexibility, the radius of gyration (R_g) for conformational compactness and solvent exposure, and molecular mechanics with generalized Born and surface area solvation (MM-GBSA) binding free energies over 800 snapshots to estimate relative binding affinities.

The average RMSD for the reference **J1Q**/Bcl-2 complex was 1.17 Å (Fig. S34, SI). The virtual complexes exhibited comparable stability, with average RMSDs of 2.82 Å (**7a**), 2.34 Å (**8a**), 2.93 Å (**8b**), 2.10 Å (**8e**), and 1.78 Å (**8f**). This suggests stable complex formation for all simulated ligands. RMSF analysis (Fig. S35A, SI) showed similar patterns for all complexes compared to **J1Q**/Bcl-2, with most residues below 2.0 Å, indicating stable interactions. Some flexibility was noted, for instance, in residue Asp34. Ligand RMSF analysis (Fig. S35B, SI) revealed dynamic repositioning during simulations. Notably, **8f** showed an average ligand RMSF of 0.80 Å, similar to **J1Q** (0.72 Å), indicating stability within the binding pocket. Radius of gyration (R_g) analysis assessed the compactness of the complexes. Average R_g values were 4.69 Å (**7a**), 5.04 Å (**8a**), 4.88 Å (**8b**), 5.01 Å (**8e**), 4.66 Å (**8f**), and, closely matching **J1Q** (4.61 Å) (Fig. S36). The comparable R_g of **8f** to **J1Q** suggests a compact, stable complex, consistent with strong binding. Solvent-accessible surface area (SASA) and hydrogen bond analyses (Fig. S37 and S38) further support the stability of the complexes. MM-GBSA calculations estimated binding free energies (Δ*G* bind) (Table 3).

The stabilization of the complexes was predominantly driven by lipophilic energies and van der Waals interactions, with additional favorable contributions from coulombic energies. The calculated average binding free energy (Δ*G*_bind) for the **J1Q**/Bcl-2 complex was -81.11 ± 3.72 kcal mol^{-1}. The binding energies for compounds **7a**, **8a**, **8b**, **8e**, and **8f**, were -52.80 ± 2.76, -48.49 ± 2.87, -54.94 ± 3.24, -66.72 ± 2.91, -84.98 ± 3.43 and kcal mol^{-1}, respectively, with an estimated uncertainty of ±5–10 kcal mol^{-1}. These values indicate energetically favorable binding. The ranking based on calculated binding energies correlates well with the observed antiproliferative activities

Table 3 MM-GBSA binding affinities (kcal mol^{-1}) for ligand-Bcl-2 interactions over 800 MD snapshots (uncertainty: ±5–10 kcal mol^{-1})[a]

Energy terms	J1Q	7a	8a	8b	8e	8f
Δ*G* bind Coulomb	−31.28 ± 3.02	−6.30 ± 1.69	−7.93 ± 1.52	−6.69 ± 2.18	−6.66 ± 1.75	−15.24 ± 3.77
Δ*G* bind covalent	2.19 ± 0.98	0.87 ± 0.78	1.01 ± 1.03	1.54 ± 1.25	0.88 ± 0.68	7.33 ± 2.40
Δ*G* bind H-bond	−0.04 ± 0.07	−0.22 ± 0.25	−0.38 ± 0.36	−0.19 ± 0.18	−0.18 ± 0.22	−1.40 ± 0.55
Δ*G* bind Lipo	−34.34 ± 1.67	−15.42 ± 1.00	−17.97 ± 1.30	−19.52 ± 1.16	−24.73 ± 1.47	−30.54 ± 1.52
Δ*G* bind packing	−2.62 ± 0.28	−4.11 ± 1.17	−4.24 ± 1.47	−5.41 ± 1.15	−3.98 ± 0.87	−4.38 ± 2.18
Δ*G* bind SelfCont	0 ± 0	0 ± 0	0 ± 0	0 ± 0	0 ± 0	0 ± 0
Δ*G* bind Solv GB	38.05 ± 3.70	12.02 ± 1.37	16.45 ± 0.91	15.75 ± 1.90	19.14 ± 2.06	22.81 ± 3.72
Δ*G* bind vdW	−53.07 ± 2.40	−39.64 ± 2.13	−35.43 ± 1.92	−40.42 ± 2.08	−51.18 ± 1.98	−63.56 ± 5.04
Δ*G* bind total	−81.11 ± 3.72	−52.80 ± 2.76	−48.49 ± 2.87	−54.94 ± 3.24	−66.72 ± 2.91	−84.98 ± 3.43

[a] Values expressed as averages ± standard deviations. Δ*G* bind Coulomb: Coulomb energy, Δ*G* bind covalent: covalent energy, Δ*G* bind H-bond: hydrogen-bonding correction, Δ*G* bind Lipo: Lipophilic energy, Δ*G* bind packing: pi–pi packing correction, Δ*G* bind SelfCont: self-contact correction, δ*g* bind Solv GB: generalized born electrostatic solvation energy, Δ*G* bind vdW: van der Waals energy, Δ*G* bind total: the relationship between energy components.

Table 4 Bcl-2 receptor-ligand contacts (≥50% simulation duration)

Ligand	Pi–pi stacking	Hydrophobic interactions	Hydrogen bonding	Salt bridge
J1Q	Phe104, Phe112	Tyr108	—	Asp111
7a	Tyr108	Phe112, Met115, Leu137, Ala149	—	—
8a	—	Tyr108, Met115, Leu137	—	—
8b	—	Phe112	Asn143	—
8e	Tyr108	Phe112, Met115	Arg139	—
8f	Phe153	Met115	Gln114, Val133	—

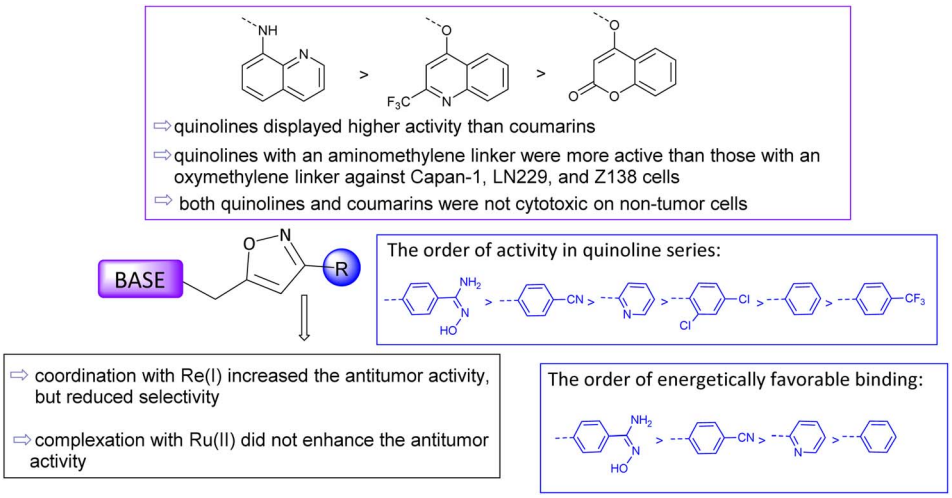

Fig. 5 Structure–activity relationship insights for antitumor activity and Bcl-2 binding of novel quinoline (**7a–e**, **8a–f**) and coumarin-based isoxazole derivatives (**9a–e**) and their rhenium(I) (**7b$_{Re}$**, **9b$_{Re}$**) and ruthenium(II) complexes (**7b$_{Ru}$**, **9b$_{Ru}$**).

against HL-60, Z-138, and to a lesser extent, DND-41 cell lines (Table 1). Importantly, the calculated binding energy of **8f** (−84.98 kcal mol^{-1}) slightly exceeded that of the potent reference inhibitor **J1Q** (−81.11 kcal mol^{-1}, IC$_{50}$ = 1.3 μM), suggesting that **8f** possesses strong Bcl-2 inhibitory potential. Further analysis of persistent receptor-ligand contacts throughout the simulation (Table 4) revealed specific interactions, including π–π stacking, hydrophobic interactions, and hydrogen bonds, which contribute to the stabilization of each complex.

The antiproliferative activity findings, along with molecular modeling studies, provided insights into the structural activity relationship (Fig. 5). While the length of the linker has not been optimized, the aminomethylene linker generally showed better activity than the oxymethylene linker in quinoline derivatives **8a–f**. Coordination with Re(I) further enhanced the antiproliferative activity, most notably against pancreatic adenocarcinoma and hematologic malignancies. However, these organometallic complexes also displayed considerable cytotoxicity toward non-cancerous PBMC cells. In the quinoline series, substitution at the 3-position of the isoxazole ring significantly influenced both cytotoxic potency and Bcl-2 binding affinity. The trend in binding free energies was consistent with the observed antiproliferative activity (**8f** > **8e** > **8b** > **8a**). Compound **8f**, containing a (4-amidoxime)phenyl-substituted isoxazole moiety, exhibited the highest and most selective activity, in agreement with its most favorable binding free energy.

2.2.4. Principal component analysis of MD trajectories. To investigate the essential dynamics and conformational heterogeneity of the Bcl-2 complexes, we performed Principal Component Analysis (PCA) on the Cα atoms from the 1000 ns MD trajectories. PCA provides a reduced-dimensional representation of protein motion by identifying the dominant collective motions that contribute most to the overall conformational variance.[62] The eigenvalue decomposition revealed that the essential subspace of protein dynamics could be captured by a limited number of principal components. For all complexes studied, the first three principal components (PCs) accounted for 65–80% of the total variance (Fig. 6A–F), with PC1 contributing 35–48%, PC2 contributing 15–22%, and PC3 contributing 8–12% of the total motion. This dimension reduction indicates that the protein dynamics are dominated by a few collective motions rather than random fluctuations. Analysis of the reference **J1Q**/Bcl-2 complex showed well-defined conformational clusters in the PC1–PC2 subspace (Fig. 6A), with a cumulative variance of 78% captured by the first 10 PCs. The trajectory exhibited a rapid equilibration phase (0–200 ns, shown in black) followed by stable sampling within a confined conformational space (200–1000 ns, transitioning from brown to orange). This pattern suggests that the **J1Q** inhibitor stabilizes specific conformational states of Bcl-2. Remarkably, compound **8f** demonstrated a similar PCA profile (Fig. 6B), with comparable variance distribution (PC1: 45%, PC2: 18%, PC3: 10%) and cluster formation. The

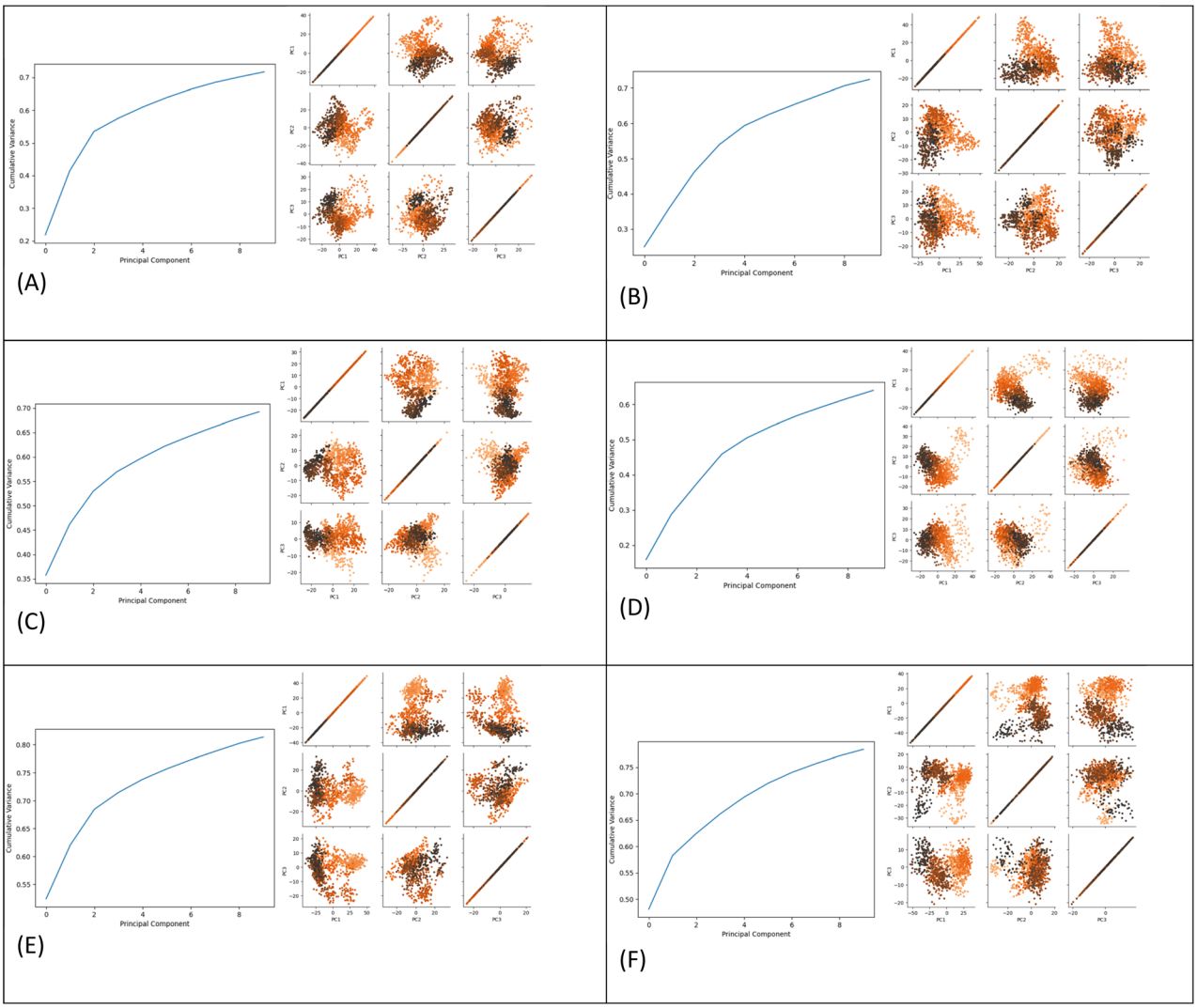

Fig. 6 Principal component analysis of MD trajectories. (A–F) Combined representation showing cumulative variance plots (left panels) and PC1 *vs.* PC2 *vs.* PC3 scatter plots (right panels) for complexes of Bcl-2 with (A) **J1Q**, (B) **8f**, (C) **8e**, (D) **8b**, (E) **8a**, and (F) **7a**. Color gradient represents simulation time from 0 ns (black) through 500 ns (brown) to 1000 ns (orange). The cumulative variance plots show the contribution of the first 10 principal components to the total variance.

conformational space explored by **8f** overlapped significantly with that of **J1Q**, particularly in the PC1–PC2 projection, where both compounds occupied similar regions cantered around PC1 $\approx$ 10 Å and PC2 $\approx$ −5 Å. This conformational similarity supports our MM-GBSA findings that **8f** exhibits comparable binding affinity to the reference inhibitor. In contrast, compounds **7a**, **8a**, **8b**, and **8e** showed distinct PCA signatures.

Compound **8e** (Fig. 6C) displayed broader conformational sampling along PC1, suggesting greater flexibility in the binding site. The bimodal distribution along PC2 indicates the presence of two major conformational substates that interconvert during the simulation. Compounds **7a** and **8a** (Fig. 6E and F) exhibited the most dispersed conformational landscapes, with continuous drift along PC1 throughout the simulation (evident from the color gradient), indicating less stable binding modes. Projection of the trajectories onto the first principal component revealed the time-dependent conformational changes (Fig. S39). The **J1Q** and **8f** complexes showed minimal drift after initial equilibration, maintaining PC1 values within ±5 Å of their mean positions. Conversely, **7a** exhibited progressive drift along PC1, with values ranging from −25 to +40 Å over the simulation period, suggesting continuous conformational reorganization. The PCA-derived root means square fluctuations (RMSF) along the first three PCs correlated well with the binding site residues identified in our contact analysis (r = 0.82), confirming that the essential dynamics captured by PCA are relevant to ligand binding. Residues showing high contributions to PC1 included Phe104, Tyr108, and Met115, which form the hydrophobic pocket accommodating the ligand's aromatic moieties. These PCA results provide mechanistic insights into the differential binding stabilities observed in our MM-GBSA calculations. The confined conformational sampling of **8f**, similar to **J1Q**, indicates effective stabilization of the Bcl-2 binding site, while the broader

sampling of other compounds suggests suboptimal protein–ligand complementarity. This conformational analysis further validates compound **8f** as a promising Bcl-2 inhibitor with binding characteristics comparable to the clinically relevant reference compound. Molecular dynamics simulation trajectories for all studied complexes are provided as supplementary videos. Each video displays the 1000 ns simulation compressed to 1 minute and 50 seconds, showing the protein backbone (cartoon representation) and ligand (stick representation) evolution. Key interacting residues are highlighted, and the time progression is indicated. Videos were generated using Schrödinger Maestro (Version 2024-1) with trajectory snapshots taken every 1.0 ns. Video S1: **J1Q**/Bcl-2 reference complex (PDB: 6QGK); Video S2: compound **8f**/Bcl-2 complex; Video S3: compound **8e**/Bcl-2 complex; Video S4: compound **8b**/Bcl-2 complex; Video S5: compound **8a**/Bcl-2 complex; Video S6: compound **7a**/Bcl-2 complex.

3. Conclusions

Quinoline (**7a–e**, **8a–f**) and coumarin (**9a–e**) derivatives of 3-aryl-substituted isoxazoles, featuring oxymethylene and aminomethylene linkers, were synthesized by 1,3-dipolar cycloaddition of quinoline (**4** and **5**) and coumarin (**6**) alkynes and corresponding nitrile oxides obtained *in situ* from *N*-hydroxybenzimidoyl chlorides **3a–e**. Quinoline (**7b**) and coumarin (**9b**) derivatives containing a 3-(pyridinyl)isoxazole moiety were also used as ligands for the preparation of rhenium(I) and ruthenium(II) complexes. Antiproliferative activity assays revealed that quinoline derivatives (**8a–f**) with aminomethylene linkers exhibited higher activity compared to coumarin-based isoxazole derivatives (**9a–e**). Among the quinoline series, the 4-amidoxime phenyl-substituted quinoline **8f** showed the most pronounced and selective activity against pancreatic adenocarcinoma cells (Capan-1) ($IC_{50} = 4.7$ μM), T-cell leukemia (DND-41) ($IC_{50} = 2.3$ μM), acute myeloid leukemia (HL-60) ($IC_{50} = 2.8$ μM) and non-Hodgkin's lymphoma (Z-138) ($IC_{50} = 2.1$ μM). Both quinoline (**7a–e**, **8a–f**) and coumarin isoxazole (**9a–e**) derivatives showed no cytotoxicity towards non-cancerous cells. To further explore the influence of alternative 5-membered heterocycles on antiproliferative activity, replacement of isoxazole with triazole, thiazole and pyrazole ring will be carried out at a later stage. Rhenium tricarbonyl complexes (**7b$_{Re}$**, **9b$_{Re}$**) exhibited strong activity but lacked selectivity, whereas their ruthenium analogs (**7b$_{Ru}$**, **9b$_{Ru}$**) were inactive against all evaluated human tumor cell lines. Molecular docking studies suggest that the antiproliferative activity of compound **8f** may, at least in part, be mediated through Bcl-2 inhibition. Since compound **8f** exhibited low cytotoxicity ($IC_{50} > 100$ μM) in peripheral blood mononuclear cells from healthy donors, its selective and potent cytostatic activity against pancreatic adenocarcinoma, acute lymphoblastic leukemia, and acute myeloid leukemia cells, along with its high permeability and moderate clearance rate highlight its potential as a promising lead compound against both solid and hematological malignancies. Further studies are warranted to validate the anti-cancer potential of compound **8f** as a novel Bcl-2 inhibitor.

4. Experimental part

4.1. Materials and methods

The reactions were conducted using standard glassware, and all reagents were used as received from commercial suppliers without further purification. Reaction progress was monitored *via* thin-layer chromatography (TLC) on silica gel 60F254 plates (Merck, Darmstadt, Germany), with spot visualization performed under UV light at 254 nm. Purification of the synthesized compounds was achieved through column chromatography using silica gel (0.063–0.2 mm, Fluka, Buchs, Switzerland). The ^{1}H and ^{13}C NMR spectra were recorded in DMSO-d_6 at 298 K using a Bruker 300 or 600 MHz NMR spectrometer (Bruker Biospin, Rheinstetten, Germany). Chemical shifts were referenced to the DMSO signal at δ 2.50 ppm for ^{1}H NMR and δ 39.50 ppm for ^{13}C NMR. Melting points of the compounds were determined with a Kofler micro hot-stage apparatus (Reichert, Wien, Austria). The IR spectra of all compounds were recorded using a PerkinElmer Spectrum ONE FT-IR spectrometer equipped with a Universal UATR Sampling Accessory, covering the spectral range of 3500–500 cm^{-1}. The UV–Vis absorption spectra were measured in HPLC-grade acetonitrile at 25 °C using a Varian Cary 50 spectrophotometer. Elemental composition was analyzed using a PerkinElmer 2400 Series II CHNS analyzer, yielding values within 0.5% of theoretical predictions. Benzaldehyde oxime (**2a**),[63] picolinaldehyde oxime (**2b**),[64] 4-(trifluoromethyl)benzaldehyde oxime (**2c**),[65] 2,4-dichlorobenzaldehyde oxime (**2d**),[66] 4-((hydroxyimino)methyl)benzonitrile (**2e**),[63] *N*-hydroxybenzimidoyl chloride (**3a**),[48] *N*-hydroxypicolinimidoyl chloride (**3b**),[51] *N*-hydroxy-4-(trifluoromethyl)benzimidoyl chloride (**3c**),[50] 2,4-dichloro-*N*-hydroxybenzimidoyl chloride (**3d**),[49] 4-cyano-*N*-hydroxybenzimidoyl chloride (**3e**),[52] 4-(prop-2-yn-1-yloxy)-2-(trifluoromethyl)quinoline (**4**),[43] *N*-(prop-2-yn-1-yl)quinolin-8-amine (**5**),[45] 4-(prop-2-yn-1-yloxy)-2*H*-chromen-2-one (**6**)[43] were synthesized using literature procedures.

4.2. Synthesis of compounds

4.2.1. General procedure for the synthesis of quinoline- (7a–e, 8a–e) and coumarin- (9a–e) isoxazole derivatives. A solution of the corresponding propargylated quinoline (**4**, **5**) or coumarin (**6**) in dichloromethane (10 mL) was treated with the corresponding *N*-hydroxybenzimidoyl chloride **3a–e** (1.2 equiv.) and triethylamine (TEA, 10 equiv.) at room temperature. The mixture was then stirred under reflux for 12 hours. Upon completion, the solvent was removed under reduced pressure, and the residue was purified by column chromatography (CH_2Cl_2 : MeOH = 50 : 1) to yield the target compounds.

*4.2.1.1. 3-Phenyl-5-(((2-(trifluoromethyl)quinolin-4-yl)oxy) methyl)isoxazole (**7a**).* Compound **7a** was prepared according to the general procedure from 4-(prop-2-yn-1-yloxy)-2-(trifluoromethyl)-2*H*-quinoline **4** (300.0 mg, 1.2 mmol), (*Z*,*E*)-*N*-hydroxybenzimidoyl chloride **3a** (222.1 mg, 1.4 mmol) and TEA (1.2 g, 1.6 mL, 11.9 mmol). Compound **7a** was isolated as a white powder (418 mg, 94%, m.p = 150–152 °C). ^{1}H NMR (600 MHz, DMSO-d_6) (δ/ppm): 8.33 (dd, $J = 8.4$, 0.8 Hz, 1H, H-5), 8.13

(d, J = 8.4 Hz, 1H, H-8), 7.93 (ddd, J = 8.4, 5.7, 2.1 Hz, 3H, H-Ph, H-7), 7.77 (m, 1H, H-6), 7.67 (s, 1H, H-3), 7.54 (m, 3H, H-Ph), 7.39 (s, 1H, H-isoxazole), 5.82 (s, 2H, CH_2). ^{13}C NMR (151 MHz, DMSO-d_6) (δ/ppm): 167.31, 162.13, 161.92, 147.82 (q, J_{CF_3} = 33.7 Hz), 147.43, 131.64, 130.43, 129.15, 128.39, 128.15, 126.72, 121.86, 121.46 (q, J_{CF_3} = 275.6 Hz), 120.93, 102.74, 98.26, 61.94. Calc. for $C_{20}H_{13}F_3N_2O_2$: C, 64.87; H, 3.54; N, 7.56; Exp. C, 64.81; H, 3.58; N, 7.59%.

*4.2.1.2. 3-(Pyridin-2-yl)-5-(((2-(trifluoromethyl)quinolin-4-yl) oxy)methyl)isoxazole (**7b**).* Compound **7b** was prepared according to the general procedure from 4-(prop-2-yn-1-yloxy)-2-(trifluoromethyl)-2*H*-quinoline **4** (500.0 mg, 2.0 mmol), (*Z*,*E*)-*N*-hydroxypicolinimidoyl chloride **3b** (373.9 mg, 2.4 mmol) and TEA (2.0 g, 2.8 mL, 19.9 mmol). Compound **7b** was isolated as a white powder (699 mg, 95%, m.p. = 164–167 °C). ^{1}H NMR (300 MHz, DMSO-d_6) (δ/ppm): 8.74 (d, J = 4.6 Hz, 1H, H-6′), 8.29 (d, J = 8.0 Hz, 1H, H-5), 8.13 (d, J = 8.4 Hz, 1H, H-8), 8.07 (d, J = 7.8 Hz, 1H, H-3′), 8.09 (m, 2H, H-7, H-4′), 7.76 (t, J = 7.4 Hz, 1H, H-6), 7.69 (s, 1H, H-3), 7.55 (m, 1H, H-5′), 7.32 (s, 1H, H-isoxazole), 5.86 (s, 2H, CH_2). ^{13}C NMR (75 MHz, DMSO-d_6) (δ/ppm): 167.49, 163.03, 161.88, 150.02, 147.80 (q, J_{CF_3} = 33.9 Hz), 147.42, 147.20, 137.60, 131.62, 129.14, 128.43, 125.27, 121.76, 121.47, 121.45 (q, J_{CF_3} = 275.6 Hz), 103.46, 98.22 (q, J_{CF_3} = 2.1 Hz), 61.65. Calc. for $C_{19}H_{12}F_3N_3O_2$: C, 61.46; H, 3.26; N, 11.32; Exp. C, 61.57; H, 3.20; N, 11.38%.

*4.2.1.3. 3-(4-(Trifluoromethyl)phenyl)-5-(((2-(trifluoromethyl) quinolin-4-yl)oxy)methyl)isoxazole (**7c**).* Compound **7c** was prepared according to the general procedure from 4-(prop-2-yn-1-yloxy)-2-(trifluoromethyl)-2*H*-quinoline **4** (500.0 mg, 2.0 mmol), (*Z*,*E*)-*N*-hydroxy-4-(trifluoromethyl)benzimidoyl chloride **3c** (536.5 mg, 2.4 mmol) and TEA (2.0 g, 2.8 mL, 19.9 mmol). Compound **7c** was isolated as a white powder (438 mg, 50%, m.p. = 171–173 °C). ^{1}H NMR (600 MHz, DMSO-d_6) (δ/ppm): 8.35 (d, J = 8.3 Hz, 1H, H-5), 8.19 (d, J = 8.0 Hz, 2H, H-Ph), 8.15 (d, J = 8.4 Hz, 1H, H-8), 7.93 (t, J = 8.9 Hz, 3H, H-Ph, H-7), 7.78 (t, J = 7.5 Hz, 1H, H-6), 7.69 (s, 1H, H-3), 7.53 (s, 1H, H-isoxazole), 5.87 (s, 2H, CH_2). ^{13}C NMR (151 MHz, DMSO-d_6) (δ/ppm): 167.96, 161.88, 161.14, 147.83 (q, J_{CF_3} = 33.9 Hz), 147.43, 132.07, 131.63, 130.43 (q, J_{CF_3} = 31.8 Hz), 129.15, 128.38, 127.56, 126.08 (q, J_{CF_3} = 3.9 Hz), 124.26 (q, J_{CF_3} = 272.1 Hz), 122.12 (q, J_{CF_3} = 275.7 Hz), 121.84, 120.91, 102.92, 98.26, 61.95. Calc. for $C_{21}H_{12}F_6N_2O_2$: C, 57.54; H, 2.76; N, 6.39; Exp. C, 57.50; H, 2.79; N, 6.42%.

*4.2.1.4. 3-(2,4-Dichlorophenyl)-5-(((2-(trifluoromethyl) quinolin-4-yl)oxy)methyl)isoxazole (**7d**).* Compound **7d** was prepared according to the general procedure from 4-(prop-2-yn-1-yloxy)-2-(trifluoromethyl)-2*H*-quinoline **4** (200.0 mg, 0.8 mmol), (*Z*,*E*)-2,4-dichloro-*N*-hydroxybenzimidoyl chloride **3d** (214.5 mg, 1.0 mmol) and TEA (805.7 mg, 1.1 mL, 8.0 mmol). Compound **7d** was isolated as a white powder (148 mg, 42%, m.p. = 161–163 °C). ^{1}H NMR (600 MHz, DMSO-d_6) (δ/ppm): 8.28 (dd, J = 8.4, 1.3 Hz, 1H, H-5), 8.13 (d, J = 8.3 Hz, 1H, H-8), 7.92 (ddd, J = 8.5, 6.9, 1.7 Hz, 1H, H-7), 7.86 (d, J = 2.1 Hz, 1H, H-6′), 7.77 (m, 2H, H-6, H-3′), 7.68 (s, 1H, H-3), 7.60 (dd, J = 8.4, 2.1 Hz, 1H, H-5′), 7.29 (s, 1H, H-isoxazole), 5.86 (s, 2H, CH_2); ^{13}C NMR (151 MHz, DMSO-d_6) (δ/ppm): 166.81, 161.84, 159.99, 147.79 (q, J_{CF_3} = 33.8 Hz), 147.43, 135.64, 132.92, 132.34, 131.64, 129.98, 129.16, 128.44, 128.02, 126.43, 121.78, 121.46 (q, J_{CF_3} = 275.7 Hz), 120.91, 105.97, 98.29, 61.60. Calc. for $C_{20}H_{11}Cl_2F_3N_2O_2$: C, 54.69; H, 2.52; N, 6.38; Exp. C, 54.62; H, 2.58; N, 6.41%.

*4.2.1.5. 4-(5-(((2-(Trifluoromethyl)quinolin-4-yl)oxy)methyl) isoxazol-3-yl)benzonitrile (**7e**).* Compound **7e** was prepared according to the general procedure from 4-(prop-2-yn-1-yloxy)-2-(trifluoromethyl)-2*H*-quinoline **4** (100.0 mg, 0.4 mmol), (*Z*,*E*)-4-cyano-*N*-hydroxybenzimidoyl chloride **3e** (86.6 mg, 0.5 mmol) and TEA (402.8 mg, 0.5 mL, 4.0 mmol). Compound **7e** was isolated as a white powder (75 mg, 48%, m.p. = 183–184 °C). ^{1}H NMR (600 MHz, DMSO-d_6) (δ/ppm): 8.32 (m, 1H, H-5), 8.15 (m, 3H, H-8, H-Ph), 8.03 (m, 2H, H-Ph), 7.93 (ddd, J = 8.4, 6.9, 1.5 Hz, 1H, H-7), 7.77 (ddd, J = 8.2, 6.9, 1.2 Hz, 1H, H-6), 7.67 (s, 1H, H-3), 7.53 (s, 1H, H-isoxsazole), 5.85 (s, 2H, CH_2). ^{13}C NMR (151 MHz, DMSO-d_6) (δ/ppm): ^{13}C NMR (151 MHz, DMSO-d_6) (δ/ppm): 168.13, 161.89, 161.07, 147.85 (q, J_{CF_3} = 33.8 Hz), 147.45, 133.18, 132.47, 131.68, 129.18, 128.43, 127.57, 121.90, 121.87 (q, J_{CF_3} = 276.3 Hz), 120.92, 118.40, 112.91, 102.96, 98.31. Calc. for $C_{21}H_{12}F_3N_3O_2$: C, 63.80; H, 3.06; N, 10.63; Exp. C, 63.85; H, 3.11; N, 10.73%.

*4.2.1.6. 3-Phenyl-5-((quinolin-8-yl-azaneyl)methyl)isoxazole (**8a**).* Compound **8a** was prepared according to the general procedure from *N*-(prop-2-yn-1-yl)quinolin-8-amine **5** (100.0 mg, 0.5 mmol), (*Z*,*E*)-*N*-hydroxybenzimidoyl chloride **3a** (102.5 mg, 0.7 mmol) and TEA (555.3 mg, 0.8 mL, 5.5 mmol). Compound **8a** was isolated as a white powder (156 mg, 94%, m.p. = 104–105 °C). ^{1}H NMR (600 MHz, DMSO-d_6) (δ/ppm): 8.79 (dd, J = 4.2, 1.7 Hz, 1H, H-2), 8.24 (dd, J = 8.3, 1.7 Hz, 1H, H-4), 7.83 (m, 2H, H-Ph), 7.53 (dd, J = 8.3, 4.2 Hz, 1H, H-3), 7.47 (m, 3H, H-Ph), 7.36 (t, J = 7.9 Hz, 1H, H-6), 7.24 (t, J = 6.5 Hz, 1H, NH), 7.13 (dd, J = 8.2, 1.0 Hz, 1H, H-7), 6.91 (s, 1H, H-isoxazole), 6.77 (dd, J = 7.7, 0.9 Hz, 1H, H-5), 4.78 (d, J = 6.5 Hz, 2H, CH_2). ^{13}C NMR (151 MHz, DMSO-d_6) (δ/ppm): 172.07, 161.75, 147.18, 143.64, 137.59, 136.00, 130.12, 129.04, 128.53, 128.28, 127.59, 126.55, 121.82, 114.28, 104.95, 100.11, 38.75. Calc. for $C_{19}H_{15}N_3O$: C, 75.73; H, 5.02; N, 13.94; Exp. C, 75.76; H, 4.99; N, 13.97%.

*4.2.1.7. N-((3-(Pyridin-2-yl)isoxazol-5-yl)methyl)quinolin-8-amine (**8b**).* Compound **8b** was prepared according to the general procedure from *N*-(prop-2-yn-1-yl)quinolin-8-amine **5** (100.0 mg, 0.5 mmol), (*Z*,*E*)-*N*-hydroxypicolinimidoyl chloride **3b** (103.1 mg, 0.7 mmol) and TEA (555.3 mg, 0.7 mL, 5.5 mmol). Compound **8b** was isolated as a white powder (136 mg, 82%, m.p. = 208–210 °C). ^{1}H NMR (600 MHz, DMSO-d_6) (δ/ppm): 8.80 (dd, J = 4.2, 1.7 Hz, 1H, H-2), 8.65 (ddd, J = 4.9, 1.7, 1.0 Hz, 1H, H-6′), 8.25 (dd, J = 8.3, 1.7 Hz, 1H, H-4), 7.98 (dt, J = 7.9, 1.1 Hz, 1H, H-3′), 7.93 (td, J = 7.7, 1.8 Hz, 1H, H-5′), 7.54 (dd, J = 8.3, 4.2 Hz, 1H, H-3), 7.48 (ddd, J = 7.5, 4.9, 1.2 Hz, 1H, H-4′), 7.37 (t, J = 7.9 Hz, 1H, H-6), 7.27 (t, J = 6.7 Hz, 1H, NH), 7.14 (dd, J = 8.2, 0.9 Hz, 1H, H-7), 6.83 (s, 1H, H-isoxazole), 6.81 (m, 1H, H-6), 4.82 (d, J = 6.7 Hz, 2H, CH_2). ^{13}C NMR (151 MHz, DMSO-d_6) (δ/ppm): 172.42, 162.69, 149.88, 147.55, 147.24, 143.55, 137.61, 137.49, 136.03, 128.29, 127.57, 125.02, 121.84, 121.24, 114.35, 105.12, 100.70, 38.52. Calc. for $C_{18}H_{14}N_4O$: C, 71.51; H, 4.67; N, 18.53; Exp. C, 71.48; H, 4.62; N, 18.58%.

*4.2.1.8. N-((3-(4-(Trifluoromethyl)phenyl)isoxazol-5-yl)methyl) quinolin-8-amine (**8c**).* Compound **8c** was prepared according to the general procedure from *N*-(prop-2-yn-1-yl)quinolin-8-amine

5 (100.0 mg, 0.5 mmol), (*E*,*Z*)-*N*-hydroxy-4-(trifluoromethyl) benzimidoyl chloride **3c** (147.3 mg, 0.7 mmol) and TEA (555.3 mg, 0.8 mL, 5.5 mmol). Compound **8c** was isolated as a white powder (125 mg, 62%, m.p. = 104–106 °C). ^{1}H NMR (600 MHz, DMSO-d_6) (δ/ppm): 8.79 (dd, J = 4.2, 1.7 Hz, 1H, H-2), 8.24 (dd, J = 8.3, 1.7 Hz, 1H, H-4), 8.06 (d, J = 8.1 Hz, 2H, H-Ph), 7.83 (d, J = 8.3 Hz, 2H H-Ph), 7.53 (dd, J = 8.3, 4.2 Hz, 1H, H-3), 7.36 (t, J = 7.9 Hz, 1H, H-6), 7.27 (t, J = 6.5 Hz, 1H, NH), 7.14 (dd, J = 8.2, 0.9 Hz, 1H, H-7), 7.03 (s, 1H, H-isoxazole), 6.77 (dd, J = 7.7, 0.9 Hz, 1H, H-6), 4.80 (s, 2H, CH_2). ^{13}C NMR (151 MHz, DMSO-d_6) (δ/ppm): 172.80, 160.77, 147.19, 143.61, 137.60, 136.00, 132.46, 130.13 (q, J_{CF_3} = 31.8 Hz), 128.29, 127.58, 127.40, 125.97 (q, J_{CF_3} = 3.4 Hz), 123.94 (q, J_{CF_3} = 272.4 Hz), 121.83, 114.32, 104.93, 100.38, 38.76. Calc. for $C_{20}H_{14}F_3N_3O$: C, 65.04; H, 3.82; N, 11.38; Exp. C, 65.09; H, 3.78; N, 11.42%.

*4.2.1.9. N-((3-(2,4-Dichlorophenyl)isoxazol-5-yl)methyl) quinolin-8-amine (**8d**).* Compound **8d** was prepared according to the general procedure from *N*-(prop-2-yn-1-yl)quinolin-8-amine **5** (100.0 mg, 0.5 mmol), (*E*,*Z*)-2,4-dichloro-*N*-hydroxybenzimidoyl chloride **3d** (147.8 mg, 0.7 mmol) and TEA (555.3 mg, 0.8 mL, 5.5 mmol). Compound **8d** was isolated as a white powder (126 mg, 62%, m.p. = 166–167 °C). ^{1}H NMR (600 MHz, DMSO-d_6) (δ/ppm): 8.78 (dd, J = 4.1, 1.6 Hz, 1H, H-2), 8.24 (dd, J = 8.3, 1.6 Hz, 1H, H-4), 7.80 (d, J = 2.1 Hz, 1H, H-6′), 7.69 (d, J = 8.4 Hz, 1H, H-3′), 7.54 (td, J = 8.5, 3.1 Hz, 2H, H-5′, H-3), 7.37 (t, J = 7.9 Hz, 1H, H-6), 7.24 (t, J = 6.6 Hz, 1H, NH), 7.14 (d, J = 7.6 Hz, 1H, H-7), 6.81 (d, J = 5.3 Hz, 2H, H-5, H-isoxazole), 4.81 (d, J = 6.6 Hz, 2H, CH_2). ^{13}C NMR (151 MHz, DMSO-d_6) (δ/ppm): 171.72, 159.60, 147.21, 143.57, 137.56, 136.01, 135.31, 132.77, 132.20, 129.91, 128.27, 127.91, 127.56, 126.80, 121.82, 114.35, 105.05, 103.12, 56.88. Calc. for $C_{19}H_{13}Cl_2N_3O$: C, 61.64; H, 3.54; N, 11.35; Exp. C, 61.68; H, 3.50; N, 11.39%.

*4.2.1.10. 4-(5-((Quinolin-8-ylamino)methyl)isoxazol-3-yl) benzonitrile (**8e**).* Compound **8e** was prepared according to the general procedure from *N*-(prop-2-yn-1-yl)quinolin-8-amine **5** (100.0 mg, 0.5 mmol), (*Z*,*E*)-4-cyano-*N*-hydroxybenzimidoyl chloride **3e** (118.8 mg, 0.7 mmol) and TEA (555.3 mg, 0.8 mL, 5.5 mmol). Compound **8e** was isolated as a white powder (100 mg, 61%, m.p. = 149–152 °C). ^{1}H NMR (600 MHz, DMSO-d_6) (δ/ppm): 8.79 (dd, J = 4.2, 1.7 Hz, 1H, H-2), 8.24 (dd, J = 8.3, 1.7 Hz, 1H, H-4), 8.05 (m, 2H, H-Ph), 7.94 (m, 2H, H-Ph), 7.53 (dd, J = 8.3, 4.2 Hz, 1H, H-3), 7.35 (t, J = 7.9 Hz, 1H, H-6), 7.26 (t, J = 6.5 Hz, 1H, NH), 7.13 (dd, J = 8.2, 0.9 Hz, 1H, H-7), 7.05 (s, 1H, H-isoxazole), 6.74 (m, 1H, H-5), 4.80 (d, J = 6.5 Hz, 2H, CH_2). ^{13}C NMR (151 MHz, DMSO-d_6) (δ/ppm): 172.95, 160.68, 147.20, 143.60, 137.60, 136.01, 133.05, 132.86, 128.30, 127.59, 127.40, 121.84, 118.40, 114.34, 112.57, 104.93, 100.45, 38.78. Calc. for $C_{20}H_{14}N_4O$: C, 73.61; H, 4.32; N, 17.17; Exp. C, 73.68; H, 4.27; N, 17.21%.

*4.2.1.11. 4-((3-Phenylisoxazol-5-yl)methoxy)-2H-chromen-2-one (**9a**).* Compound **9a** was prepared according to the general procedure from 4-(prop-2-yn-1-yloxy)-2*H*-chromen-2-one **6** (300.0 mg, 1.5 mmol), (*Z*,*E*)-*N*-hydroxybenzimidoyl chloride **3a** (279.8 mg, 1.8 mmol) and TEA (1.5 g, 2.1 mL, 15.0 mmol). Compound **9a** was isolated as a white powder (216 mg, 45%, m.*p* = 183–192 °C). ^{1}H NMR (600 MHz, DMSO-d_6) (δ/ppm): 7.93 (dt, J = 5.1, 2.0 Hz, 2H, H-Ph), 7.90 (dd, J = 8.0, 1.8 Hz, 1H, H-5), 7.69 (ddd, J = 8.7, 7.3, 1.8 Hz, 1H, H-7), 7.54 (m, 3H, H-Ph), 7.44 (d, J = 8.3 Hz, 1H, H-8), 7.38 (m, 2H, H-isoxazole/H-6), 6.17 (s, 1H, H-3), 5.64 (s, 2H, CH_2). ^{13}C NMR (151 MHz, DMSO-d_6) (δ/ppm): 166.74, 163.98, 162.12, 161.36, 152.76, 133.00, 130.46, 129.16, 128.10, 126.71, 124.35, 122.99, 116.49, 114.82, 102.93, 91.72, 61.88. Calc. for $C_{19}H_{13}NO_4$: C, 71.47; H, 4.10; N, 4.39; Exp. C, 71.42; H, 4.13; N, 4.41%.

*4.2.1.12. 4-((3-(Pyridin-2-yl)isoxazol-5-yl)methoxy)-2H-chromen-2-one (**9b**).* Compound **9b** was prepared according to the general procedure from 4-(prop-2-yn-1-yloxy)-2*H*-chromen-2-one **6** (100.0 mg, 0.5 mmol), (*Z*,*E*)-*N*-hydroxypicolinimidoyl chloride **3b** (93.8 mg, 0.6 mmol) and TEA (505.5 mg, 0.7 mL, 5.0 mmol). Compound **9b** was isolated as a white powder (152 mg, 95%, m.p. = 201–204 °C). ^{1}H NMR (600 MHz, DMSO-d_6) (δ/ppm): 8.74 (dd, J = 4.8, 0.7 Hz, 1H, H-6′), 8.06 (dd, J = 4.9, 4.0 Hz, 1H, H-4′), 7.99 (td, J = 7.7, 1.8 Hz, 1H, H-5), 7.85 (dd, J = 7.9, 1.5 Hz, 1H, H-3′), 7.68 (ddd, J = 8.6, 7.4, 1.6 Hz, 1H, H-7), 7.55 (ddd, J = 7.5, 4.8, 1.1 Hz, 1H, H-5′), 7.43 (m, 1H, H-8), 7.38 (m, 1H, H-6), 7.33 (s, 1H, H-isoxazole), 6.19 (s, 1H, H-3), 5.67 (s, 2H, CH_2). ^{13}C NMR (151 MHz, DMSO-d_6) (δ/ppm): 166.92, 161.37, 152.76, 150.04, 147.18, 137.65, 133.00, 125.32, 124.39, 122.92, 121.50, 116.50, 114.81, 103.75, 91.72, 61.58. IR (ATR)/cm^{-1}: 3081, 2981, 1720, 1609, 1567, 1375, 1254, 1111, 839, 782, 621. Calc. for $C_{18}H_{12}N_2O_4$: C, 67.50; H, 3.78; N, 8.75; Exp. C, 67.54; H, 3.72; N, 8.79%.

*4.2.1.13. 4-((3-(4-(Trifluoromethyl)phenyl)isoxazol-5-yl) methoxy)-2H-chromen-2-one (**9c**).* Compound **9c** was prepared according to the general procedure from 4-(prop-2-yn-1-yloxy)-2*H*-chromen-2-one **6** (100.0 mg, 0.5 mmol), (*Z*,*E*)-*N*-hydroxy-4-(trifluoromethyl)benzimidoyl chloride **3c** (134.0 mg, 0.5 mmol) and TEA (505.5 mg, 0.7 mL, 5.0 mmol). Compound **9c** was isolated as a white powder (111 mg, 57%, m.p. = 140–208 °C). ^{1}H NMR (600 MHz, DMSO-d_6) (δ/ppm): 8.17 (d, J = 8.2 Hz, 2H, H-Ph), 7.90 (m, 3H, H-Ph, H-5), 7.74 (m, 1H, H-7), 7.51 (s, 1H, H-isoxazole), 7.43 (d, J = 8.3 Hz, 1H, H-8), 7.39 (t, J = 7.6 Hz, 1H, H-6), 6.17 (s, 1H, H-3), 5.66 (s, 2H, CH_2). ^{13}C NMR (151 MHz, DMSO-d_6) (δ/ppm): 167.39, 163.95, 161.36, 161.14, 152.77, 132.96, 132.04, 130.55 (q, J_{CF_3} = 32.0 Hz), 127.58, 126.10 (J_{CF_3} = 3.6 Hz), 124.35, 123.95 (q, J_{CF_3} = 272.4 Hz), 122.98, 116.50, 114.80, 103.14, 91.72, 61.88. Calc. for $C_{20}H_{12}F_3NO_4$: C, 62.02; H, 3.12; N, 3.62; Exp. C, 62.08; H, 3.18; N, 3.58%.

*4.2.1.14. 4-((3-(2,4-Dichlorophenyl)isoxazol-5-yl)methoxy)-2H-chromen-2-one (**9d**).* Compound **9d** was prepared according to the general procedure from 4-(prop-2-yn-1-yloxy)-2*H*-chromen-2-one **6** (100.0 mg, 0.5 mmol), (*Z*,*E*)-2,4-dichloro-*N*-hydroxybenzimidoyl chloride **3d** (134.5 mg, 0.6 mmol) and TEA (505.5 mg, 0.7 mL, 5.0 mmol). Compound **9d** was isolated as a white powder (138 mg, 70%, m.p. = 166–189 °C). ^{1}H NMR (600 MHz, DMSO-d_6) (δ/ppm): 7.88 (d, J = 2.0 Hz, 1H, H-6′), 7.86 (dd, J = 8.0, 1.8 Hz, 1H, H-3′), 7.78 (d, J = 8.4 Hz, 1H, H-3′), 7.68 (m, 1H, H-7), 7.62 (dd, J = 8.4, 2.2 Hz, 1H, H-5′), 7.44 (dd, J = 8.4, 1.2 Hz, 1H, H-8), 7.38 (m, 1H, H-6), 7.29 (s, 1H, H-isoxazole), 6.19 (s, 1H, H-3), 5.67 (s, 2H, CH_2). ^{13}C NMR (151 MHz, DMSO-d_6) (δ/ppm): 166.28, 163.94, 161.34, 160.00, 152.74, 135.66, 133.00, 132.93, 132.37, 130.00, 128.03, 126.40, 124.38, 122.93, 116.50, 114.77, 106.08, 91.74, 61.57. Calc. for

$C_{19}H_{11}Cl_2NO_4$: C, 58.79; H, 2.86; N, 3.61; Exp. C, 58.81; H, 2.83; N, 3.65%.

*4.2.1.15. 4-(5-(((2-Oxo-2H-chromen-4-yl)oxy)methyl)isoxazol-3-yl)benzonitrile (**9e**).* Compound **9e** was prepared according to the general procedure from 4-(prop-2-yn-1-yloxy)-2*H*-chromen-2-one **6** (100.0 mg, 0.5 mmol), (*Z*,*E*)-4-cyano-*N*-hydroxybenzimidoyl chloride **3e** (108.3 mg, 0.6 mmol) and TEA (505.5 mg, 0.7 mL, 5.0 mmol). Compound **9e** was isolated as a white powder (148 mg, 86%, m.p. = 221–223 °C). ^{1}H NMR (600 MHz, DMSO-d_6) (δ/ppm): 8.13 (dd, J = 6.4, 1.9 Hz, 2H, H-Ph), 8.02 (dd, J = 6.3, 2.0 Hz, 2H, H-Ph), 7.88 (dd, J = 8.0, 1.7 Hz, 1H, H-5), 7.68 (m, 1H, H-7), 7.52 (s, 1H, H-isoxazole), 7.42 (d, J = 8.4 Hz, 1H, H-8), 7.38 (m, 1H, H-6), 6.16 (s, 1H, H-3), 5.66 (s, 2H, CH_2). ^{13}C NMR (151 MHz, DMSO-d_6) (δ/ppm): 167.51, 163.91, 161.32, 161.02, 152.74, 133.13, 132.98, 132.39, 127.53, 124.31, 122.95, 118.34, 116.47, 114.78, 112.88, 103.10, 91.76, 61.87. Calc. for $C_{20}H_{12}N_2O_4$: C, 69.77; H, 3.51; N, 8.14; Exp. C, 69.79; H, 3.54; N, 8.16%.

4.2.2. Synthesis of amidoxime-substituted derivative (*Z*)-*N*′-hydroxy-4-(5-((quinolin-8-ylamino)methyl)isoxazol-3-yl) benzimidamide (8f). The cyano derivative **8e** (100 mg, 0.3 mmol) was suspended in a mixture of methanol and dimethylformamide (2 : 1, v/v) and heated to 100 °C. Triethylamine (Et_3N, 3 equiv., 93.0 mg, 0.12 mL, 0.9 mmol) and hydroxylamine hydrochloride ($NH_2OH \times HCl$, 3 equiv., 63.8 mg, 0.9 mmol) were then added and the reaction mixture was stirred for 6 hours. After cooling to room temperature, the mixture was diluted with water and the resulting precipitate was collected by filtration. Compound **8f** was isolated as a white powder (49 mg, 42%, m.p. = 223–225 °C). ^{1}H NMR (600 MHz, DMSO-d_6) (δ/ppm): 9.77 (s, 1H, OH), 8.79 (dd, J = 4.2, 1.7 Hz, 1H, H-2), 8.24 (dd, J = 8.3, 1.6 Hz, 1H, H-4), 7.83 (m, 2H, H-Ph), 7.77 (d, J = 8.5 Hz, 2H, H-Ph), 7.53 (dd, J = 8.3, 4.2 Hz, 1H, H-3), 7.36 (t, J = 7.9 Hz, 1H, H-6), 7.24 (t, J = 6.6 Hz, 1H, NH), 7.14 (m, 1H, H-7), 6.94 (s, 1H, H-isoxazole), 6.77 (m, 1H, H-6), 5.88 (s, 2H, NH_2), 4.78 (d, J = 6.4 Hz, 2H, CH_2). ^{13}C NMR (151 MHz, DMSO-d_6) (δ/ppm): 172.14, 161.39, 150.17, 150.14, 147.18, 143.64, 137.59, 136.00, 134.81, 128.78, 128.29, 127.60, 126.31, 125.88, 121.82, 114.28, 104.93, 100.13, 38.76. Calc. for $C_{20}H_{17}N_5O_2$: C, 66.84; H, 4.77; N, 19.49; Exp. C, 66.88; H, 4.73; N, 19.53%.

4.2.3. General procedure for the synthesis of Re(I) complexes. A solution of the ligand **7b** or **9b** in chloroform was combined with $Re(CO)_5Cl$ (1 equiv.) and the reaction mixture was stirred under reflux in the dark for 12 hours. After completion, the solvent was evaporated under reduced pressure. After completion, the reaction mixture was allowed to cool to room temperature and the volume was reduced to induce the formation of a fine precipitate. The precipitate was collected by filtration and dried.

*4.2.3.1. Complex **7b$_{Re}$**.* Complex **7b$_{Re}$** was prepared according to the general procedure from ligand **7b** (30.0 mg, 0.08 mmol) and $Re(CO)_5Cl$ (29.3 mg, 0.08 mmol). Compound **7b$_{Re}$** was isolated as a yellow powder (40 mg, 92%, m.p. > 250 °C). ^{1}H NMR (600 MHz, DMSO-d_6) (δ/ppm): 9.09 (dt, J = 5.3, 1.2 Hz, 1H, H-6′), 8.65 (dt, J = 7.8, 1.1 Hz, 1H, H-3′), 8.44 (td, J = 7.8, 1.5 Hz, 1H, H-4′), 8.37 (dd, J = 8.4, 1.4 Hz, 1H, H-5), 8.17 (d, J = 8.5 Hz, 1H, H-8), 8.07 (s, 1H, H-isoxazole), 7.96 (ddd, J = 8.5, 6.8, 1.5 Hz, 1H, H-7), 7.84 (m, 2H, H-6, H-5′), 7.71 (s, 1H, H-3), 6.07 (d, J = 4.7 Hz, 2H, CH_2). ^{13}C NMR (151 MHz, DMSO-d_6) (δ/ppm): 197.44 (CO), 196.28 (CO), 188.17 (CO), 171.75, 165.01, 162.14, 154.55, 148.35 (q, J_{CF_3} = 33.8 Hz), 147.98, 147.963, 147.41, 141.51, 132.26, 129.74, 129.52, 129.03, 126.64, 122.23, 121.92 (q, J_{CF_3} = 274.8 Hz), 104.50, 98.93 (q, J_{CF_3} = 2.5 Hz), 62.50. IR (ATR)/cm^{-1}: 2981, 2021, 1981, 1895, 1572, 1368, 1278, 1119, 924, 82, 782. Calc. for. $C_{22}H_{13}ClF_3N_3O_5Re$: C, 38.97; H, 1.93; N, 6.20; Exp. C, 38.82; H, 1,99; N, 6.29%.

*4.2.3.2. Complex **9b$_{Re}$**.* Complex **9b$_{Re}$** was prepared according to the general procedure from ligand **9b** (30.0 mg, 0.08 mmol) and $Re(CO)_3Cl$ (29.3 mg, 0.08 mmol). Compound **9b$_{Re}$** was isolated as a yellow powder (35 mg, 82%, m.p. > 250 °C). ^{1}H NMR (600 MHz, DMSO-d_6) (δ/ppm): 9.09 (d, J = 5.4 Hz, 1H, H-6′), 8.64 (d, J = 7.8 Hz, 1H, H-3′), 8.44 (t, J = 7.8 Hz, 1H, H-4′), 8.06 (s, 1H, H-isoxazole), 7.94 (d, J = 7.8 Hz, 1H, H-5), 7.85 (m, 1H, H-5′), 7.72 (t, J = 7.7 Hz, 1H, H-7), 7.47 (d, J = 8.2 Hz, 1H, H-8), 7.43 (t, J = 7.6 Hz, 1H, H-6), 6.20 (s, 1H, H-3), 5.87 (d, J = 7.1 Hz, 2H, CH_2). ^{13}C NMR (151 MHz, DMSO-d_6) (δ/ppm): 196.34 (CO), 195.21 (CO), 187.07 (CO), 170.07, 163.90, 163.13, 160.67, 153.47, 152.20, 146.29, 140.43, 132.55, 128.45, 125.54, 123.82, 122.31, 116.00, 114.11, 103.53, 91.48, 61.37. IR (ATR)/cm^{-1}: 2981, 2031, 1957, 1924, 1889, 1721, 1627, 1373, 1112, 941, 830, 771. Calc. for. $C_{21}H_{12}ClN_2O_7Re$: C, 40.29; H, 1.93; N, 4.48; Exp. C, 40.35; H, 1.82; N, 4.58%.

4.2.4. General procedure for the synthesis of Ru(II) complexes. A solution of ligands **7b** or **9b** in methanol (5–10 mL) was treated with Ru(II) complexes $[Ru(benzene)Cl_2]_2$. The reaction mixture was stirred for 24 hours at room temperature. After completion, the solvent was removed under reduced pressure and the product was purified by column chromatography (CH_2Cl_2 : MeOH = 20 : 1).

*4.2.4.1. Complex **7b$_{Ru}$**.* Complex **7b$_{Ru}$** was prepared according to the general procedure from ligand **7b** (30.0 mg, 0.08 mmol) and $[Ru(benzene)Cl_2]_2$ (39.6 mg, 0.07 mmol). Compound **7b$_{Ru}$** was isolated as a red powder (11 mg, 25%, m.p. > 250 °C). ^{1}H NMR (600 MHz, DMSO-d_6) (δ/ppm): 9.72 (ddd, J = 5.7, 1.4, 0.8 Hz, 1H, H-6′), 8.59 (ddd, J = 7.8, 1.4, 0.8 Hz, 1H, H-3′), 8.38 (m, 2H, H-4′, H-5), 8.18 (dt, J = 8.4, 0.9 Hz, 1H, H-8), 8.06 (s, 1H, H-isoxazole), 7.97 (ddd, J = 8.4, 6.9, 1.5 Hz, 1H, H-7), 7.89 (ddd, J = 7.8, 5.6, 1.5 Hz, 1H, H-5′), 7.83 (ddd, J = 8.2, 6.9, 1.2 Hz, 1H, H-3), 7.75 (s, 1H), 6.31 (s, 5H, H-Ph), 6.07 (m, 2H, CH_2). ^{13}C NMR (151 MHz, DMSO-d_6) (δ/ppm): 172.44, 161.57, 156.96, 147.84 (d, J = 33.8 Hz), 147.48, 146.38, 140.62, 131.81, 129.26, 128.57, 127.99, 125.99, 121.76, 121.45 (q, J = 276.3 Hz), 120.82, 104.09, 98.49 (q, J = 2.6 Hz), 87.62, 86.43, 61.89. IR (ATR)/cm^{-1}: 2292, 1924, 1589, 1437, 1372, 1280, 1124, 1095, 925, 839, 787. Calc. for. $C_{25}H_{19}ClF_3N_3O_2Ru$: C, 51.16; H, 3.26; N, 7.16; Exp. C, 51.25; H, 3.19; N, 7.24%.

*4.2.4.2. Complex **9b$_{Ru}$**.* Complex **9b$_{Ru}$** was prepared according to the general procedure from ligand **9b** (30.0 mg, 0.08 mmol) and $[Ru(benzene)Cl_2]_2$ (39.6 mg, 0.08 mmol). Compound **9b$_{Ru}$** was isolated as a red powder (12 mg, 29%, m.p. > 250 °C). ^{1}H NMR (600 MHz, DMSO-d_6) (δ/ppm): 9.71 (d, J = 5.4 Hz, 1H, H-6′), 8.57 (d, J = 7.7 Hz, 1H, H-3′), 8.39 (t, J = 7.4 Hz, 1H, H-4′), 8.06 (s, 1H, H-isoxazole), 7.50 (m, 2H, H-5, H-7), 7.68 (m, 1H, H-5′), 7.47 (d, J = 8.3 Hz, 1H, H-8), 7.43 (t, J = 7.6 Hz, 1H, H-6), 6.31

(s, 5H, H-Ph), 6.25 (s, 1H, H-3), 5.88 (d, $J = 7.2$ Hz, 1H, CH_2). 13C NMR (151 MHz, DMSO-d_6) (δ/ppm): 171.84, 163.69, 161.54, 161.28, 156.98, 152.78, 146.35, 140.62, 133.18, 128.01, 125.99, 124.43, 122.91, 116.61, 114.67, 104.26, 92.15, 86.45, 61.80. IR (ATR)/cm^{-1}: 2981, 1628, 1437, 1372, 1280, 1124, 1095, 925, 839. Calc. for. $C_{24}H_{18}ClN_2O_4Ru$: C, 53.89; H, 3.39; N, 5.24; Exp. C, 53.94; H, 3.31; N, 5.29%.

4.3. Antiproliferative activity

4.3.1. Cell culture and reference compounds. The human cancer cell lines (Capan-1, HCT-116, NCI-H460, LN-229, HL-60, K-562, and Z-138) were obtained from the American Type Culture Collection (ATCC), while the DND-41 cell line was procured from the Deutsche Sammlung von Mikroorganismen und Zellkulturen (DSMZ). The culture media were sourced from Gibco Life Technologies, and supplemented with 10% fetal bovine serum (HyClone). Etoposide, which was used as reference inhibitor, was acquired from Selleckchem, and all stock solutions were prepared in dimethyl sulfoxide (DMSO).

4.3.2. Proliferation assays. Adherent cell line Capan-1 was plated at a density of 500 cells per well, while HCT-116, NCI-H460, and LN-229 were plated at 1500 cells per well in 384-well tissue culture plates. Following an overnight incubation, the cells were exposed to seven different concentrations of the test compounds ranging from 100 to 0.006 μM. Suspension cell lines HL-60, K-562, and Z-138 were seeded at 2500 cells per well, and the DND-41 cell line was seeded at 5500 cells per well in 384-well culture plates containing the same concentration points of test compounds. After 72 hours of incubation with the compounds, cell viability was assessed using the CellTiter 96® AQueous One Solution Cell Proliferation Assay (MTS) reagent according to the manufacturer's instructions (final assay concentrations of 333 μg per mL MTS and 25 μM PMS). Absorbance was measured at 490 nm using a SpectraMax Plus 384, and the optical density values were utilized to determine the 50% inhibitory concentration (IC_{50}). Each compound underwent testing in at least two independent experiments.

4.3.3. Cell viability of normal PBMC. Buffy coat preparations sourced from healthy donors were acquired from the Blood Transfusion Center (biobank Red Cross Flanders number M20210510A) in Leuven, Belgium. Peripheral blood mononuclear cells (PBMC) were separated using density gradient centrifugation over Lymphoprep (density: 1.077 g mL^{-1}) from Nycomed. These cells were then cultured in cell culture medium (RPMI, Gibco) supplemented with 10% FBS. The PBMC were seeded at a density of 28 000 cells per well in 384-well tissue culture plates containing the test compounds at concentrations ranging from 100 to 0.006 μM. Following a 72-hour incubation period, cell viability was assessed using the same MTS cell viability assay. Each compound was evaluated in two separate experiments, utilizing PBMC from two distinct healthy donors.

4.4. ADME profiling

Permeability testing was done on Madin–Darby canine epithelial cells over-expressing human MDR1 gene, coding for *P*-glycoprotein (MDCKII-MDR1; obtained from Solvo Biotechnology, Hungary). Cells were prepared for transport studies by seeding on 96-well cell culture inserts (Millipore, MA, USA) in a concentration of 0.25×10^6 cells per mL. The cells were cultured to confluence for 3 days before use in permeability experiment. On the day of experiment, the cell monolayers were washed and equilibrated with transport medium (DPBS, pH 7.4 containing 1% DMSO) for 30 min (37 °C, 5% CO_2, 95% humidity). Test compounds' solutions consisted of test substance (10 μM) in D-PBS medium containing lucifer yellow (100 μM) and 1% DMSO. Transport assays were conducted in apical to basolateral (A2B) and basolateral to apical (B2A) directions, respectively. Monolayers were incubated with the compound solution for 60 min at 37 °C under gentle agitation. Apical and basolateral compartments were sampled on a Freedom EVO 200 (Tecan, Männedorf, CH) at the end of the transport experiment, while donor solutions were also sampled at the beginning of the experiment in order to determine initial concentration. Test substance concentrations in both compartments were determined by LC-MS/MS. Lucifer yellow, a fluorescent marker for the paracellular membrane transport, was used as the control of cell monolayer integrity. Metabolic stability was assessed in mouse liver microsomes (Corning, USA). Compounds (final concentration of 1 μM, <0.1% DMSO v/v) were incubated in duplicate in phosphate buffer (50 mM, pH 7.4) at 37 °C together with mouse liver microsomes in the absence and presence of the NADPH regenerating system (0.5 mM nicotinamide adenine dinucleotide phosphate, 5 mM glucose-6-phosphate, 1.5 U mL^{-1} glucose-6-phosphate dehydrogenase and 0.5 mM magnesium chloride). Incubation was done for 1 h at 37 °C. Sampling was performed on a Freedom EVO 200 (Tecan, Männedorf, CH) at 0, 10, 20, 30, 45 and 60 min. The reaction was stopped by 3 volumes of a mixture of ACN/MeOH (2 : 1) containing internal standard (diclofenac), centrifuged and obtained supernatants further analyzed using LC-MS/MS. Metabolic activity of microsomes was verified by simultaneous analysis of several assay controls (testosterone, propranolol, caffeine). The *in vitro* half-life ($t_{1/2}$) was calculated using GraphPad Prism non-linear regression of % parent compound remaining *versus* time. *In vitro* clearance (Clint), expressed as μL min^{-1} mg^{-1}, was estimated from the *in vitro* half-life ($t_{1/2}$), and normalized for the protein amount in the incubation mixture. Obtained *in vitro* clearance was further scaled to predicted *in vivo* hepatic clearance, assuming 52.5 mg of protein per gram of liver, mouse liver weight/body weight of 85.7 g kg^{-1} and mouse liver blood flow (LBF) of 131 mL min^{-1} kg^{-1}.

4.5. Molecular modeling

4.5.1. Software. Schrödinger Maestro (Version 2024-1) from Schrödinger LLC, USA, was utilized.

4.5.2. Protein preparation. The crystal structure of Bcl-2 complexed with **J1Q** ((*S*)-1-(2-(3-(aminomethyl)-1,2,3,4-tetrahydroisoquinoline-2-carbonyl)phenyl)-*N*,*N*-dibutyl-5-methyl-1*H*-pyrazole-3-carboxamide, PDB code: 6QGK, $IC_{50} = 1.3$ μM)[67] was retrieved from the Protein Data Bank (PDB). The structure was prepared using the protein preparation tool[68] implemented

in Schrödinger Maestro 2024-1. Hydrogen atoms and any missing side chains were added while maintaining ions or water molecules in the X-ray structures. The protonation state and tautomeric forms of the amino acids were optimized using PROPKA tool at pH 7.0.[69] Finally, the potential energy of the prepared structures was minimized using the OPLS4 force field.[70]

4.5.3. Ligand preparation. The structures of **8f**, **8e**, **8b**, **8a**, and **7a** were drawn using the 2D sketcher in the Schrödinger Suite. The compounds were prepared using the LigPrep module and then energy-minimized with the OPLS4 force field.[70] All possible tautomeric forms and stereoisomers were generated at pH 7.4 ± 1.0 using Epik.[68] The output was then used as input for molecular docking.

4.5.4. Molecular docking and rescoring. Molecular docking was performed using the Glide program in Standard Precision (SP) mode.[71] The grid box was generated around the co-crystalized inhibitor (PDB code: 6QGK) with an inner box of 10 × 10 × 10 Å in size employing the receptor grid generation module. To validate the docking protocol, the co-crystallized inhibitor was re-docked in Glide and reproduced its binding mode with an RMSD value of 0.45 Å (Fig. 4). Conformational sampling was enhanced by a factor of 4 during conformer generation and expanded sampling was used for the selection of initial poses. A maximum of 100 docking poses were calculated for each ligand. The generated poses were then rescored using Molecular Mechanics Generalized Born Surface Area (MM-GBSA) to estimate the binding free energy of each pose.[72] Finally, the top poses, sorted by MMGBSA binding free energy values, were analyzed by visual inspection and further examined in MD simulation studies. Cross-validation protocol: to validate the reliability and reproducibility of our docking protocol, we implemented a comprehensive cross-validation strategy. First, the co-crystallized inhibitor **J1Q** (PDB: 6QGK, $IC_{50} = 1.3$ μM) was extracted from the binding site and redocked using Glide Standard Precision (SP) mode. Conformational sampling was enhanced by a factor of 4, with expanded sampling enabled for initial pose selection and 100 maximum poses retained per ligand. The redocking successfully reproduced the crystallographic binding mode with an RMSD of 0.45 Å (Fig. S33), confirming the accuracy of our geometric sampling and scoring protocol.

4.5.5. Molecular dynamics (MD) simulation. Molecular dynamics (MD) simulations of the virtual complexes for bioactive compounds **8f**, **8e**, **8b**, **8a**, and **7a**, were performed using the Desmond-v7.7 package (Schrödinger LLC) with the OPLS4 force field.[73] The following protocols were applied.

4.5.6.1. System setup. Ligand–protein complexes were solvated in an orthorhombic box using the SPC water model with a buffer distance of 10 Å. Sodium/chloride ions were added to neutralize the system.

4.5.6.2. Equilibration. Before performing the production simulation, the default Desmond protocol for energy minimization and model relaxation was applied.[74] Energy minimization was conducted using steepest descent algorithm over 2000 iterations. Equilibration under the NPT ensemble (constant number of particles, pressure [1 bar], and temperature [300 K]) was performed for 100 ps to stabilize solvent density and system pressure.

4.5.6.3. Production runs. Production simulations were conducted under the NPT ensemble (constant number of particles, pressure, and temperature [300 K]) for 1000 ns per system, with trajectories saved every 1000 ps. The NPT ensemble is implemented to maintain constant pressure and temperature. This approach enables dynamic solvent density adjustments, ensuring physiologically relevant conditions for ligand–protein interactions. By incorporating pressure equilibration, the method enhances thermodynamic sampling of binding site dynamics while accommodating bulk solvent effects.[74]

4.5.6.4. Analysis parameters. Root-mean-square deviation (RMSD) and root-mean-square fluctuation (RMSF) were calculated for backbone atoms and ligand atoms, respectively. Solvent-accessible surface area (SASA), radius of gyration (R_g), and hydrogen-bond occupancy were analyzed using Schrödinger Maestro's Simulation Interaction Diagram tool. MM-GBSA binding free energies were calculated over 800 snapshots using the Prime v7.5 module.[75–77]

4.5.6.5. Validation. The reproducibility of simulations was confirmed by Duplicate runs for the co-crystallized complex (**J1Q**, PDB: 6QGK).

Conflicts of interest

There are no conflicts to declare.

Data availability

The data supporting this article have been included as part of the supplementary information (SI). Supplementary information: ^{1}H NMR, ^{13}C NMR, FTIR, UV-Vis spectra, and molecular docking studies with Bcl-2. See DOI: https://doi.org/10.1039/d5ra05483d.

Acknowledgements

We greatly appreciate the financial support of the Croatian Science Foundation under the project HRZZ-IP-2022-10-9420.

References

1 O. Afzal, S. Kumar, M. R. Haider, M. R. Ali, R. Kumar, M. Jaggi and S. Bawa, *Eur. J. Med. Chem.*, 2015, **97**, 871–910.
2 R. Musiol, *Expert Opin. Drug Discovery*, 2017, **12**, 583–597.
3 M. Ilakiyalakshmi and A. Arumugam Napoleon, *Arabian J. Chem.*, 2022, **15**, 104168.
4 S. Jain, V. Chandra, P. Kumar Jain, K. Pathak, D. Pathak and A. Vaidya, *Arabian J. Chem.*, 2019, **12**, 4920–4946.
5 V. Pradhan, S. Salahuddin, R. Kumar, A. Mazumder, M. M. Abdullah, M. Shahar Yar, M. J. Ahsan and Z. Ullah, *Chem. Biol. Drug Des.*, 2022, **101**, 977.
6 M. Živanović, M. Selaković, A. Pavić, Ž. Selaković, B. Šolaja, J. F. Santibanez and T. Srdić-Rajić, *Chem.–Biol. Interact.*, 2024, **404**, 111281.

7 A. Božić, A. Marinković, S. Bjelogrlić, T. R. Todorović, I. N. Cvijetić, I. Novaković, C. D. Muller and N. R. Filipović, *RSC Adv.*, 2016, **6**, 104763–104781.
8 N. Chirra, H. Begum, N. P. Abburi, R. K. Bollikanda, P. Murugesan, S. Kantevari and A. D. Tangutur, *J. Mol. Struct.*, 2024, **1312**, 138677.
9 H. Begum, N. Chirra, D. Kumar, P. Murugesan, S. Kantevari and A. D. Tangutur, *Drug Dev. Res.*, 2022, **83**, 910–926.
10 M. Koley, J. Han, V. A. Soloshonok, S. Mojumder, R. Javahershenas and A. Makarem, *RSC Med. Chem.*, 2024, **15**, 10–54.
11 A. K. Yadav, R. Maharjan Shrestha and P. N. Yadav, *Eur. J. Med. Chem.*, 2024, **267**, 116179.
12 A. Thakur, R. Singla and V. Jaitak, *Eur. J. Med. Chem.*, 2015, **101**, 476–495.
13 Y. Wu, J. Xu, Y. Liu, Y. Zeng and G. Wu, *Front. Oncol.*, 2020, **10**, 1–11.
14 A. Rawat and A. Vijaya Bhaskar Reddy, *Eur. J. Med. Chem. Rep.*, 2022, **5**, 100038.
15 R. J. Roskoski, *Pharmacol. Res.*, 2024, **200**, 107059.
16 A. Saxena, S. Majee, D. Ray and B. Saha, *Bioorg. Med. Chem.*, 2024, **103**, 117681.
17 A. Aguilar-Valdés, L. G. Noriega, A. R. Tovar, M. de J. Ibarra-Sánchez, V. A. Sosa-Hernández, J. L. Maravillas-Montero and J. Martínez-Aguilar, *Biochem. Biophys. Res. Commun.*, 2021, **552**, 23–29.
18 J. E. Cortes, C. Gambacorti-Passerini, M. W. Deininger, M. J. Mauro, C. Chuah, D.-W. Kim, I. Dyagil, N. Glushko, D. Milojkovic, P. le Coutre, V. Garcia-Gutierrez, L. Reilly, A. Jeynes-Ellis, E. Leip, N. Bardy-Bouxin, A. Hochhaus and T. H. Brümmendorf, *J. Clin. Oncol.*, 2018, **36**, 231–237.
19 A. Sochacka-Ćwikła, M. Mączyński and A. Regiec, *Cancers*, 2021, **14**, 87.
20 A. Martorana, G. La Monica and A. Lauria, *Molecules*, 2020, **25**, 4279.
21 X. Zhai, G. Bao, L. Wang, M. Cheng, M. Zhao, S. Zhao, H. Zhou and P. Gong, *Bioorg. Med. Chem.*, 2016, **24**, 1331–1345.
22 C. Grülich, *Recent Results Cancer Res.*, 2014, **201**, 207–214.
23 A. P. Fay, L. Albiges and J. Bellmunt, *Expert Rev. Anticancer Ther.*, 2015, **15**, 151–156.
24 K. Feldinger and A. Kong, *Breast Cancer*, 2015, **7**, 147–162.
25 A. Al-Sheikh, M. A. Jaber, H. Khalaf, N. AlKhawaja and D. Abuarqoub, *RSC Adv.*, 2024, **14**, 3304–3313.
26 P. Y. Wen, W. K. A. Yung, K. R. Lamborn, P. L. Dahia, Y. Wang, B. Peng, L. E. Abrey, J. Raizer, T. F. Cloughesy, K. Fink, M. Gilbert, S. Chang, L. Junck, D. Schiff, F. Lieberman, H. A. Fine, M. Mehta, H. I. Robins, L. M. DeAngelis, M. D. Groves, V. K. Puduvalli, V. Levin, C. Conrad, E. A. Maher, K. Aldape, M. Hayes, L. Letvak, M. J. Egorin, R. Capdeville, R. Kaplan, A. J. Murgo, C. Stiles and M. D. Prados, *Clin. Cancer Res.*, 2006, **12**, 4899–4907.
27 H. L. Lin, H. Zhang, C. Medower, P. F. Hollenberg and W. W. Johnson, *Drug Metab. Dispos.*, 2011, **39**, 345–350.
28 S. Adhikari, P. Nath, A. Das, A. Datta, N. Baildya, A. K. Duttaroy and S. Pathak, *Biomed. Pharmacother.*, 2024, **171**, 116211.
29 N. B. Sadeer, R. Varghese, S. Ramamoorthy and G. Zengin, *Inorg. Chim. Acta*, 2024, **572**, 122294.
30 S. R. Munnangi, A. A. A. Youssef, N. Narala, P. Lakkala, S. Narala, S. K. Vemula and M. Repka, *Pharm. Res.*, 2023, **40**, 1519–1540.
31 M. Frezza, S. Hindo, D. Chen, A. Davenport, S. Schmitt, D. Tomco and Q. P. Dou, *Curr. Pharm. Des.*, 2010, **16**, 1813–1825.
32 M. Sohrabi, M. Saeedi, B. Larijani and M. Mahdavi, *Eur. J. Med. Chem.*, 2021, **216**, 113308.
33 S. Parveen, F. Arjmand and S. Tabassum, *Eur. J. Med. Chem.*, 2019, **175**, 269–286.
34 A. Marco, P. Ashoo, S. Hernández-García, P. Martínez-Rodríguez, N. Cutillas, A. Vollrath, D. Jordan, C. Janiak, F. Gandía-Herrero and J. Ruiz, *J. Med. Chem.*, 2024, **67**, 7891–7910.
35 L. Enslin, K. Purkait, M. Dalla Pozza, B. Saubaméa, P. Mesdom, H. Visser, G. Gasser and M. Schutte-Smith, *Inorg. Chem.*, 2023, **62**, 12237–12251.
36 R. Kumar, A. Thakur, S. Sachin, D. Chandra, A. Kumar Dhiman, P. Kumar Verma and U. Sharma, *Coord. Chem. Rev.*, 2024, **499**, 215453.
37 H. R. Sonawane, B. T. Vibhute, B. D. Aghav, J. V Deore and S. K. Patil, *Eur. J. Med. Chem.*, 2023, **258**, 115549.
38 P. S. Zinman, A. Welsh, R. O. Omondi, S. Khan, S. Prince, E. Nordlander and G. S. Smith, *Eur. J. Med. Chem.*, 2024, **266**, 116094.
39 K. Łyczko, A. Pogorzelska, U. Częścik, M. Koronkiewicz, J. E. Rode, E. Bednarek, R. Kawęcki, K. Węgrzyńska, A. Baraniak, M. Milczarek and J. C. Dobrowolski, *RSC Adv.*, 2024, **14**, 18080–18092.
40 A. Dritsopoulos, N. Zacharopoulos, A. E. Peyret, E. Karampella, N. Tsoureas, A. Cheilari, C. Machalia, E. Emmanouilidou, A. K. Andreopoulou, J. K. Kallitsis and A. I. Philippopoulos, *Chemistry*, 2024, **6**, 773–793.
41 S. Jakopec, L. Hamzic, L. Bočkor, I. Car, B. Perić, S. Kirin, M. Sedic and S. Raić-Malić, *Arch. Pharm.*, 2024, **357**, e2400271.
42 T. G. Kraljević, A. Harej, M. Sedić, S. K. Pavelić, V. Stepanić, D. Drenjančević, J. Talapko and S. Raić-Malić, *Eur. J. Med. Chem.*, 2016, **124**, 794–808.
43 S. Maračić, P. Grbčić, S. Shammugam, M. Radić Stojković, K. Pavelić, M. Sedić, S. Kraljević Pavelić and S. Raić-Malić, *Molecules*, 2021, **26**, 7060.
44 M. Piškor, I. Ćorić, B. Perić, K. M. Špoljarić, S. I. Kirin, L. Glavaš-Obrovac and S. Raić-Malić, *J. Inorg. Biochem.*, 2025, **262**, 112770.
45 S. Maračić, J. Lapić, S. Djaković, T. Opačak-Bernardi, L. Glavaš-Obrovac, V. Vrček and S. Raić-Malić, *Appl. Organomet. Chem.*, 2019, **33**, e4628.
46 S. Maračić, S. Jakopec, M. Piškor, M. Leventić, J. Lapić, S. Djaković, M. Cetina, L. Glavaš-Obrovac and S. Raić-Malić, *Appl. Organomet. Chem.*, 2023, **37**, e7124.
47 I. Sokol, M. Toma, M. Krnić, A. M. MacAn, D. Drenjančević, S. Liekens, S. Raić-Malić and T. G. Kraljević, *Future Med. Chem.*, 2021, **13**, 1865–1884.

48 N. C. Tran, H. Dhondt, M. Flipo, B. Deprez and N. Willand, *Tetrahedron Lett.*, 2015, **56**, 4119–4123.
49 C. Altuğ, M. Büyükbayram, Ö. Kavas and M. Z. Yavuz, *Tetrahedron*, 2014, **70**, 3590–3594.
50 L. Di Nunno, P. Vitale, A. Scilimati, L. Simone and F. Capitelli, *Tetrahedron*, 2007, **63**, 12388–12395.
51 S. Krompiec, P. Bujak, J. Malarz, M. Krompiec, Ł. Skórka, T. Pluta, W. Danikiewicz, M. Kania and J. Kusz, *Tetrahedron*, 2012, **68**, 6018–6031.
52 N. B. Gaikwad, P. Afroz, M. N. Ahmad, G. Kaul, M. Shukla, S. Nanduri, A. Dasgupta, S. Chopra and V. M. Yaddanapudi, *J. Mol. Struct.*, 2021, **1227**, 129545.
53 S. Jakopec, L. Gourdon-Grünewaldt, I. Čipor, A. Meščić Macan, B. Perić, I. Piantanida, K. Cariou, G. Gasser, S. I. Kirin and S. Raić-Malić, *Dalton Trans.*, 2023, **52**, 9482–9498.
54 R. Morales-Guevara, D. Páez-Hernández, E. Ancede-Gallardo and A. Carreño, *Int. J. Quantum Chem.*, 2025, **125**, e70005.
55 H. Roy and S. Nandi, *Curr. Pharm. Des.*, 2019, **25**, 3292–3305.
56 S. Qian, Z. Wei, W. Yang, J. Huang, Y. Yang and J. Wang, *Front. Oncol.*, 2022, **12**, 1–16.
57 R. Hamdy, S. A. Elseginy, N. I. Ziedan, A. T. Jones and A. D. Westwell, *Molecules*, 2019, **24**, 1–13.
58 M. W. Chao, H. L. Huang, W. C. HuangFu, K. C. Hsu, Y. M. Liu, Y. W. Wu, C. F. Lin, Y. L. Chen, M. J. Lai, H. Y. Lee, J. P. Liou, C. M. Teng and C. R. Yang, *Oncotarget*, 2017, **8**, 27772–27785.
59 N. Pathan, C. Aime-Sempe, S. Kitada, S. Haldar and J. C. Reed, *Neoplasia*, 2001, **3**, 70–79.
60 F. C. Rodrigues, N. V. A. Kumar, G. Hari, K. S. R. Pai and G. Thakur, *Chem. Pap.*, 2021, **75**, 5995–6008.
61 N. H. Aboalhaija, M. A. Zihlif and M. O. Taha, *Chem.–Biol. Interact.*, 2016, **250**, 12–26.
62 C. C. David and D. J. Jacobs, *Methods Mol. Biol.*, 2014, **1084**, 193–226.
63 L. Schwarz, U. Girreser and B. Clement, *Eur. J. Org. Chem.*, 2014, **2014**, 1961–1975.
64 S. Liu, W. Wei, Y. Li, X. Liu, X. Cao, K. Lei and M. Zhou, *Eur. J. Med. Chem.*, 2015, **95**, 473–482.
65 F. Yraola, S. García-Vicente, J. Fernández-Recio, F. Albericio, A. Zorzano, L. Marti and M. Royo, *J. Med. Chem.*, 2006, **49**, 6197–6208.
66 J. T. Li, X. L. Li and T. S. Li, *Ultrason. Sonochem.*, 2006, **13**, 200–202.
67 J. B. Murray, J. Davidson, I. Chen, B. Davis, P. Dokurno, C. J. Graham, R. Harris, A. Jordan, N. Matassova, C. Pedder, S. Ray, S. D. Roughley, J. Smith, C. Walmsley, Y. Wang, N. Whitehead, D. S. Williamson, P. Casara, T. Le Diguarher, J. Hickman, J. Stark, A. Kotschy, O. Geneste and R. E. Hubbard, *ACS Omega*, 2019, **4**, 8892–8906.
68 R. C. Johnston, K. Yao, Z. Kaplan, M. Chelliah, K. Leswing, S. Seekins, S. Watts, D. Calkins, J. Chief Elk, S. V Jerome, M. P. Repasky and J. C. Shelley, *J. Chem. Theory Comput.*, 2023, **19**, 2380–2388.
69 M. H. M. Olsson, C. R. SØndergaard, M. Rostkowski and J. H. Jensen, *J. Chem. Theory Comput.*, 2011, **7**, 525–537.
70 C. Lu, C. Wu, D. Ghoreishi, W. Chen, L. Wang, W. Damm, G. A. Ross, M. K. Dahlgren, E. Russell, C. D. Von Bargen, R. Abel, R. A. Friesner and E. D. Harder, *J. Chem. Theory Comput.*, 2021, **17**, 4291–4300.
71 R. A. Friesner, J. L. Banks, R. B. Murphy, T. A. Halgren, J. J. Klicic, D. T. Mainz, M. P. Repasky, E. H. Knoll, M. Shelley, J. K. Perry, D. E. Shaw, P. Francis and P. S. Shenkin, *J. Med. Chem.*, 2004, **47**, 1739–1749.
72 J. A. Bell, Y. Cao, J. R. Gunn, T. Day, E. Gallicchio, Z. Zhou, R. Levy and R. Farid, in *International Tables for Crystallography*, International Union of Crystallography, Chester, 2012, pp. 534–538, DOI: 10.1107/97809553602060000864.
73 K. J. Bowers, D. E. Chow, H. Xu, R. O. Dror, M. P. Eastwood, B. A. Gregersen, J. L. Klepeis, I. Kolossvary, M. A. Moraes, F. D. Sacerdoti, J. K. Salmon, Y. Shan and D. E. Shaw, *ACM/IEEE SC 2006 Conf.*, 2007, p. 43.
74 D. V. Nikolay, in *Computational Modeling of Biological Systems*, 2012.
75 R. Kumari, R. Kumar and A. Lynn, *J. Chem. Inf. Model.*, 2014, **54**, 1951–1962.
76 S. Pronk, S. Páll, R. Schulz, P. Larsson, P. Bjelkmar, R. Apostolov, M. R. Shirts, J. C. Smith, P. M. Kasson, D. van der Spoel, B. Hess and E. Lindahl, *Bioinformatics*, 2013, **29**, 845–854.
77 S. Siddiqui, F. Ameen, I. Jahan, S. M. Nayeem and M. Tabish, *New J. Chem.*, 2019, **43**, 4137–4151.